Report of
the Ishigaki/Miyako Campaign Experiment
for TRMM (IMCET) 1998

Preface

TRMM was successfully launched in November 1997. TRMM has a unique rain package which consists of a rain radar (PR), a microwave radiometer and a visible/infrared radiometer. The rain radar is the first spaceborne radar and was developed in Japan. A field campaign experiment for validation of TRMM, especially for the PR, was planned and conducted in 1998. The instruments are: Communications Research Laboratory's (CRL's) airborne rain radar with the same frequency of TRMM PR and ground-based radars operated by the Japan Meteorological Agency (JMA). The field was around Ishigakijima and Miyakojima Islands in the South-western island chain in Japan. There, we have an C-band radar located in Ishigakijima Island. The radar has a very good skyline over ocean and was thought to be ideal of rain observation over ocean. An enhanced radiosonde observation was also included. Simultaneous rain observation using the airborne radar, ground-based radar and PR was the main work. Though we had a good comparison in the rain patterns among radars, the result was not so conclusive as expected. The main reason is the performance of PR is much better than expected, and the accuracy of the validation is not enough to determine the accuracy of PR.

This report is on the field campaign in 1998. Though the result are still unsatisfactory, it might be good to report the activity of the field experiment and current results. We welcome any comments for this report.

We would like to express our sincere gratitude to the participants and agencies/bodies for the field experiment. JMA performed the enhance radiosonde observation, ground-based and shipborne radars observation. JMA also allowed us to use facilities in the Miyakojima Meteorological Observatory. Remote Sensing Technology Center (RESTEC) helped in logistics and also data analysis. Nakanihon Air Service, Co. Ltd., successfully operated observation flight using Beechcraft King Air aircraft with an airborne radar. Communications Research Laboratory group led by Dr. T. Kozu operated the airborne radar.

TRMM validation project scientist
Kenji Nakamura

Report of the Ishigaki/Miyako Campaign Experiment for TRMM (IMCET) 1998

Contents

1. Outline of the Ishigaki/Miyako Campaign Experiment for TRMM (IMCET)

Kenji Nakamura : TRMM validation project scientist

1.1 Outline of IMCET

Ishigakijima Island and Miyakojima Island are located in the most south-western area in Japan and are surrounded by open oceans. Since the first priority Tropical Rainfall Measuring Mission (TRMM) objective is to measure tropical rainfall over the ocean, Ishigakijima and Miyakojima area is the most suitable site for TRMM validation in Japan. The campaign experiment was conducted in this area's rainy season, that is, from the middle of May to the middle of June.

TRMM, which was launched from NASDA’s Tanegashima Space Center on November 29, 1997, is a joint venture between Japan and the US. TRMM has several rain sensors: a precipitation radar (PR), microwave and visible/infrared radiometers (TMI and VIRS), lightning sensor (LIS) and Earth radiant sensor (CERES). The PR, which was developed in Japan, is the first spaceborne rain radar and makes TRMM a unique mission.

Japan's TRMM validation activity, which emphasizes on PR validation, is closely related to the TRMM PR team. The Japan Meteorological Agency’s (JMA's) routinely accumulated data, such as AMeDAS and radar-AMeDAS composite rain maps, is used for this validation activity. Along with the routine data, a field campaign was conducted. The major field campaign was "Ishigaki/Miyako Campaign Experiment for TRMM (IMCET)." IMCET ’98 was conducted in cooperation with JMA and Communications Research Laboratory (CRL) from May 20 to June 10, 1998. In this experiment, CRL airborne multi-parameter radar (CAMPR-D) and JMA's Ishigakijima radar played the major roles. The first step in the PR validation is a radar reflectivity comparison. The rainfall rate comparison has some issues, such as the raindrop size distribution variations. Thus, we first tried to compare the radar reflectivity measured by the PR and ground-based or airborne radars. Ground-based Doppler radars are also planned to be employed in IMCET ’99. The three-dimensional radar reflectivity structure at the time of TRMM overpass is the most important data set for the PR algorithm validation. The precipitation system development itself was thus studied using enhanced sonde operation.

The PR rain estimate algorithm has many steps including measured radar reflectivity deduction and rain attenuation correction using several methods. We can validate the PR rain estimate algorithms using the three-dimensional radar reflectivity data. Profiling the dynamic structure of rain systems, such as the profile of latent heat release, is also one of the major goals of IMCET.

1.2 Experimental Field and Instruments

Under the major validation programs for the PR, IMCET’98 was conducted around

Miyakojima Island of Japan for nearly 20 days in May and June 1998. During the experiment campaign, JMA’s ground-based radars, the airborne rain radar (CAMPR-D) and a shipborne radar were employed. Enhanced radiosonde operations were also performed. CAMPR-D has a dual-beam capability. Figure 1.1 shows the coverage of JMA’s radars. The IMCET region is covered by Ishigakijima and Okinawa radars.

Specifications of JMA’s radars are shown in Table 1.1. The Okinawa radar is located at 26 deg. 08 min. North, 127 deg. 45 min. East; the Ishigakijima radar is located at 24 deg. 10 min. North, 124 deg. 20 min. East in the chain of islands in the southwest of Japan. The Miyakojima area is surrounded by ocean and is very useful for the rain observation over ocean. Since one of the PR products is the rain observation over oceans, this area is suitable for comparing satellite data with ground truth data. TRMM is the first space mission dedicated to quantitatively measuring tropical and subtropical rainfall. The major PR parameters are listed in Table 1.2. Standard products of the PR have been generated routinely at the Earth Observation Center (EOC), National Space Development Agency of Japan (NASDA) and at the Goddard Space Flight Center (GSFC), National Aeronautics and Space Administration (NASA). Figure 1.2 shows the data processing flow for the standard algorithm.

Specifications of CAMPR-D are shown in Table 1.3. CAMPR-D and the PR have similar rain measurement geometry in the sense that both observe rain from above. They also employ signals of nearly the same frequency so many aspects of the PR are expected to be validated using CAMPR-D. Another objective of this experiment was to calibrate the airborne radar for measuring the sea-surface because the sea-surface is considered to be a good calibration source.

During IMCET ’98, May 26 and 27 were the most rainy days, as can be seen clearly from GMS images in Figure 1.3. Some rain events were also experienced on May 30, 1998. Ground-based radars performed the Plan Position Indicator (PPI) scanning. The rain was monitored by the ground-based radars and the aircraft was navigated towards the rain region. Then CAMPR-D observation was conducted at the same time and location as the PR observation.

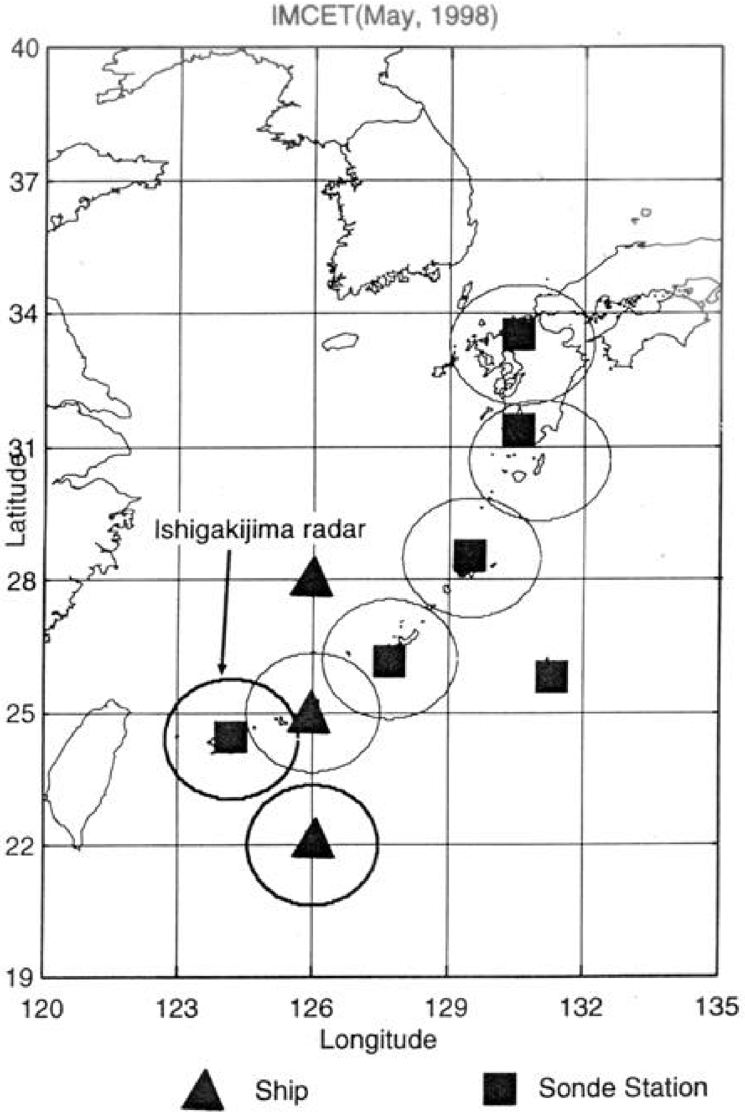

Fig. 1.1 Intensive observation area of IMCET. Circles indicate coverage of each radar

Table 1.1 Specifications of JMA's radars.

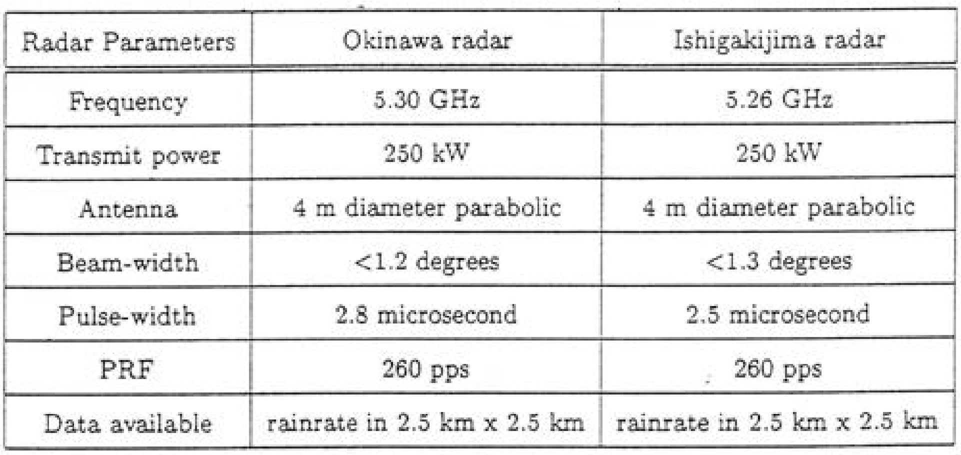

Radar Parameters	Okinawa radar	Ishigakijima radar
Frequency	5.30 GHz	5.26 GHz
Transmit power	250 kW	250 kW
Antenna	4 m diameter parabolic	4 m diameter parabolic
Beam-width	<1.2 degrees	<1.3 degrees
Pulse-width	2.8 microsecond	2.5 microsecond
PRF	260 pps	260 pps
Data available	rainrate in 2.5 km x 2.5 km	rainrate in 2.5 km x 2.5 km

Table 1.2 Major system performance and specifications of TRMM PR.

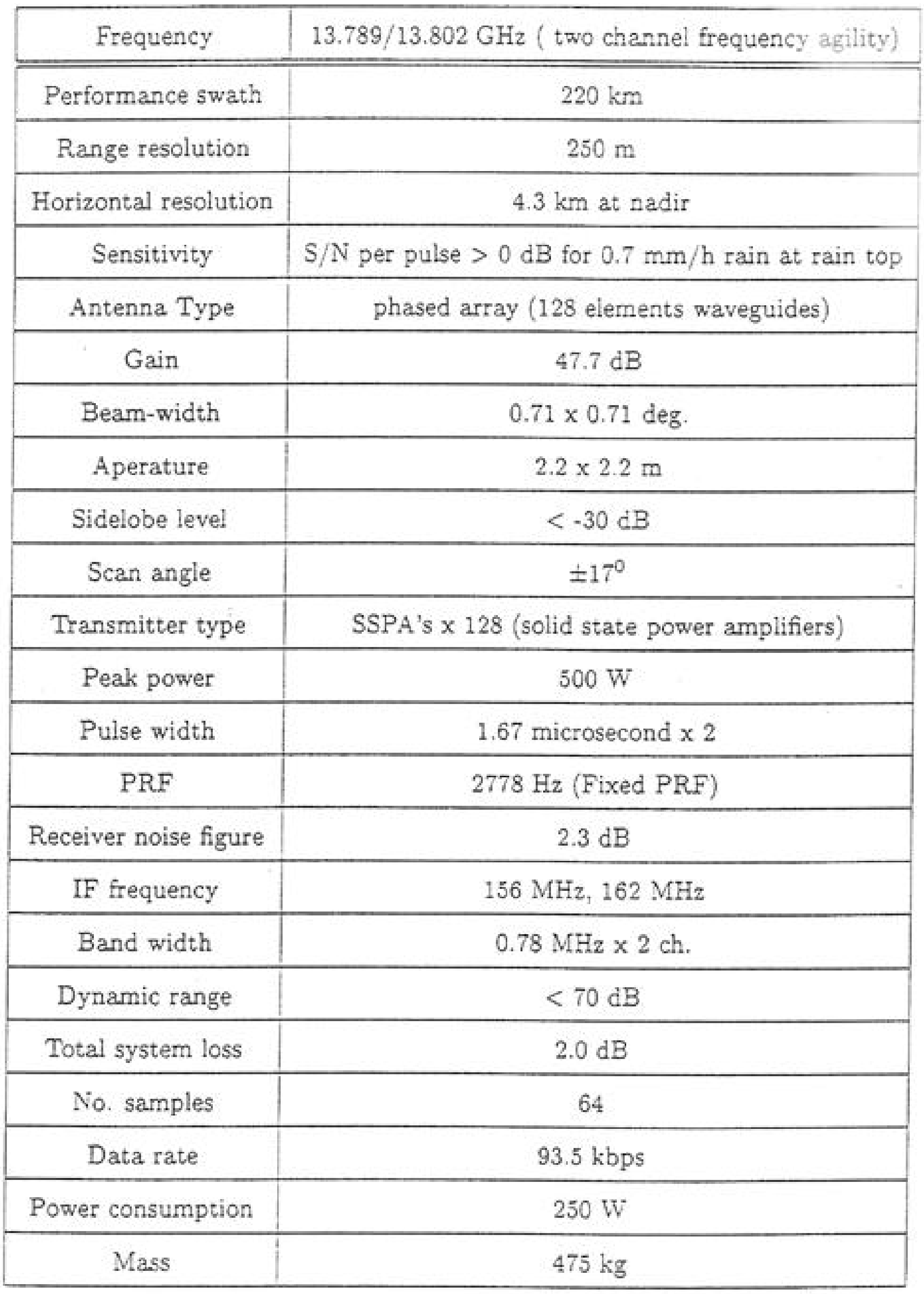

Frequency	13.789/13.802 GHz (two channel frequency agility)
Performance swath	220 km
Range resolution	250 m
Horizontal resolution	4.3 km at nadir
Sensitivity	S/N per pulse > 0 dB for 0.7 mm/h rain at rain top
Antenna Type	phased array (128 elements waveguides)
Gain	47.7 dB
Beam-width	0.71 x 0.71 deg.
Aperature	2.2 x 2.2 m
Sidelobe level	< -30 dB
Scan angle	$\pm 17^0$
Transmitter type	SSPA's x 128 (solid state power amplifiers)
Peak power	500 W
Pulse width	1.67 microsecond x 2
PRF	2778 Hz (Fixed PRF)
Receiver noise figure	2.3 dB
IF frequency	156 MHz, 162 MHz
Band width	0.78 MHz x 2 ch.
Dynamic range	< 70 dB
Total system loss	2.0 dB
No. samples	64
Data rate	93.5 kbps
Power consumption	250 W
Mass	475 kg

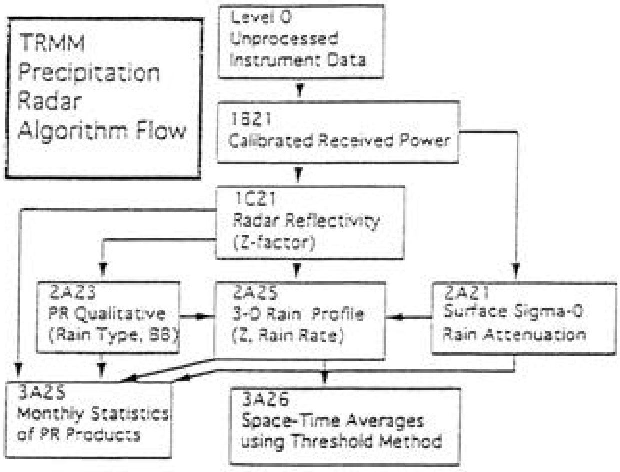

Fig. 1.2 PR standard algorithm data flow.

Table 1.3 Specifications of CAMPR-D.

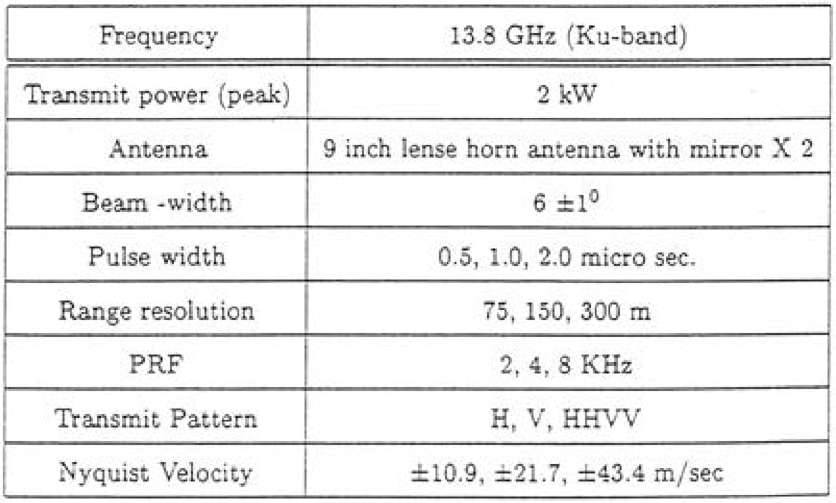

Frequency	13.8 GHz (Ku-band)
Transmit power (peak)	2 kW
Antenna	9 inch lense horn antenna with mirror X 2
Beam -width	6 ± 1^0
Pulse width	0.5, 1.0, 2.0 micro sec.
Range resolution	75, 150, 300 m
PRF	2, 4, 8 KHz
Transmit Pattern	H, V, HHVV
Nyquist Velocity	±10.9, ±21.7, ±43.4 m/sec

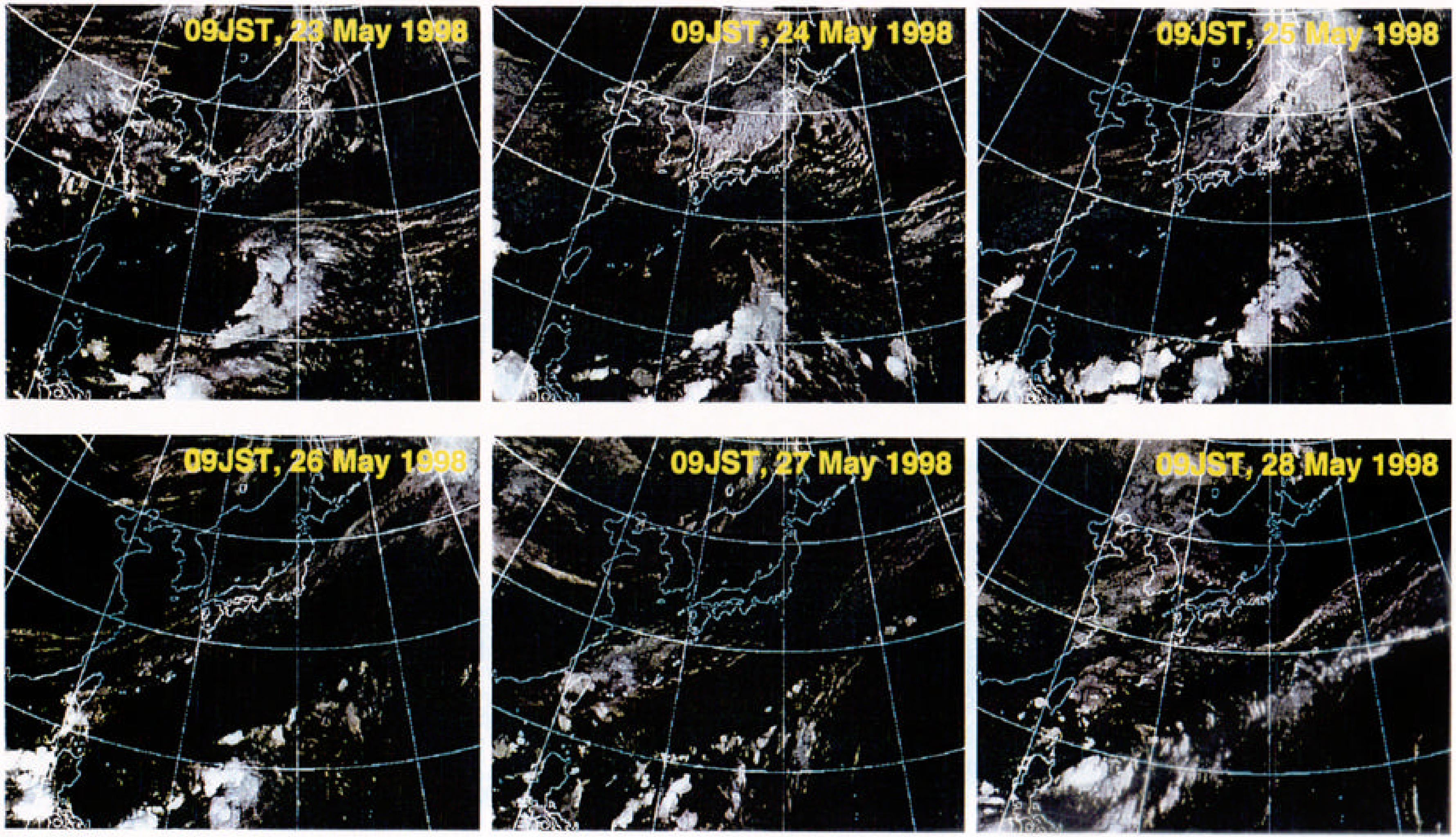

Fig. 1.3 Daily GMS images during IMCET 1998.

2. Calibration of CAMPR-D

Kenji Nakamura : Nagoya University

2.1 Sea-surface measurement by CAMPR-D

The normalized surface cross section of the ocean surface is one established source for radar system calibration. Weather radars are designed for targets uniformly distributed in pulse volume while the surface is a two-dimensional target. The exact shape of the surface echo itself is thus a complex function. The CAMPR-D antenna is designed to scan from nadir to the near horizon, which enables obtaining surface characteristics over a very wide angle with a constant antenna pattern. The flight measurements were performed on the open sea where the influences of coastlines and the bottom of the sea on the surface conditions may be neglected. The influences of clouds can nearly be neglected. We tried to select data in nearly rain-free areas. The sea-surface backscattering strongly depends on the surface wind conditions, but we do not have wind field data for that location. Furthermore, the sea-surface backscattering depends not only on the wind conditions but also on the incidence angle, polarization and wavelength. It also depends on the sea-surface slope, the swell direction relative to the wind direction, the air-sea temperature, the sea-surface temperature, the surface current, surface slicks, coastline bottom features, and internal waves.

The surface echo can be obtained at the gate with the biggest echo or an average of those gates that intersect the surface. Figure 2.1 shows the day-to-day variations in the sea-surface characteristics in nearly rain-free areas. There is some variation of measured power though the radar parameters (e.g. Pulse Repetition Frequency) are similar. As we mentioned earlier, the ocean surface is roughened by the wind and waves, and even light winds will roughen the ocean sufficiently to cause fluctuations in reflected energy. According to Jones et al. (1977) and Schroeder (1982), the σ_0 is almost constant for all wind speeds at 10 deg. incidence. CAMPR-D’s sea-surface measurements show some agreements with these results. Some data, e.g. on May 17, have systematic reduction (denoted by squares). The reason is not clear. Generally, quasi-specular scattering is considered predominant in this incident angle region (Valenzuela, 1978).

Figure 2.2 (left) shows the peak power measured by CAMPR-D for the integral mode data. Data were obtained by scanning the antenna angle over ± 30 deg. centered at the nadir. Figure 2.2 (right) shows the peak power measured by CAMPR for I, Q mode by scanning the antenna stepwise over ± 45 deg. This corresponds somewhat with integral mode data. According to Masuko et al. (1986), σ_0 increases with some power of wind speed. As we mentioned earlier, we do not have wind data for that location. Also, the aircraft changes altitude, so the peak surface echo may be poorly estimated. The aircraft roll and pitch also affect surface signatures. In our case, we did some correction for aircraft roll and selected data in nearly rain-free areas. At nadir incidence, we have a greater difference of the measured powers for two observation modes due to saturation of the radar signal for I, Q mode, as shown in Figure 2.3. The range gate ’98’ is the peak surface bin. For nearly vertical incidence, the strongest backscattering from the sea for the angles of incidence beyond about 20 deg. is governed by Bragg scattering (Uraby, 1982). The ocean surface, wave height and surface roughness can change significantly from day to day. We compared the datasets which are immediately adjacent to each other or same location when rain was absent.

Figure 2.4 shows another example of the variation of the measured relative backscattering cross section σ_0 as a function of radar incidence angle for CAMPR-D. We assumed a Gaussian antenna pattern in calculating relative σ_0, but we have some discrepancy. It also shows the backscattering cross section dependence on polarization. According to Masuko et al. (1986), for incident angles smaller than 20 deg., the σ_0 for HH polarization is slightly larger than for VV polarization because the effective reflection coefficient for HH polarization is larger than that for VV polarization. This agrees well with CAMPR-D relative σ_0 measurements.

According to Meneghini et al. (1998), the smallest standard deviations of rain-free normalized radar cross section (NRCS) over the ocean occur at incidence angles from 3 deg. to 7 deg. with a minimum of 1.36 dB at 4.26 deg. for the PR. At nadir incidence, the mean value of the NRCS is 12.91 dB with a standard deviation of 2.03. This larger standard deviation seems to be due to wind. Although the PR derived σ_0 is from global measurements, it corresponds with CAMPR-D sea-surface measurements. Figure 2.5 (a) shows ocean backscattering measurement from the PR 1C21 for the Miyakojima area during IMCET’98. The CAMPR-D antenna scans mechanically to produce a constant antenna pattern over the swath, making calibration easier. In contrast, PR scans electronically in cross-track direction. Electronic scanning generally implies greater complexity as well as difficulties in calibration due to changes in the beamwidth, and therefore changes in the radar constant with incidence angle (Meneghini and Kozu, 1990). Although the scanning direction is different, the PR measured ocean signatures, i.e., profile, are consistent with CAMPR-D sea-surface measurements as shown in Figure 2.5 (b).

2.2 Comparison of CAMPR-D and ground-based radars

We compared the intensities of rain echoes measured by CAMPR-D with those measured by JMA’s ground-based radars. We have 2.5 km × 2.5 km grid data from the ground-based radars. The horizontal resolution of the PR is nearly 4.3 km at nadir while CAMPR-D has very nice resolution data. Therefore, we have some complications in determining pairs of data for comparisons. We simply selected the pairs by matching their positions in the case of CAMPR-D (nadir) with ground-based radars. For data selection, averaging was performed over CAMPR-D samples which lie within the PR pixel size.

The comparison between Okinawa radar and CAMPR-D is shown in Figure 2.6. There seems some correlation. Figure 2.7 compares Ishigakijima radar and CAMPR-D. These seem to correlate well although there is some temporal mismatching. One reason for the discrepancy in radar comparisons might be the radar calibration factor for CAMPR-D, which was not considered in the radar equation in these analyses.

To summarize the data comparison, we found some correlations between CAMPR-D and ground-based radars.

References

Jones, W. L., L. C. Schroeder and J. L. Mitchell (1977): Aircraft measurements of the microwave scattering signature of the ocean, IEEE Trans. Antennas Propag., AP-25 (1), 52-61.

Schroeder, L. C., D. H. Boggs, G. Dome, I. M. Halberstam, W. L. Jones, W. J. Pierson and F. J. Wentz (1982): The relationship between wind vector and normalized radar cross section used to derive Seasat-A satellite scatterometer winds, J. Geophys. Res., 87 (C5), 3318-3336

Valenzuela, G. R. (1978): Theories for the interaction of electromagnetic and ocean waves - A review, Boundary Layer Meteorol., 13 (1-4), 277-293.

Masuko, H., Okamoto, K., Masanobu, S., Shuntaro N. (1986): Measurement of microwave backscattering signatures of the ocean surface using X Band and K Band airborne scatterometers. J. Geophy. Research, Vol. 91, No. C11, pp. 13065-13083.

Ulaby, F. T., Moore, R. K. and Fung, A. K. (1982): Microwave Remote Sensing Vol. II, Addison-Wesley Pub., 1064pp.

Meneghini, R., Iguchi T., Kozu, T., Okamoto, K., L. Liao, J. A. Jones (1998): Use of the surface reference technique for path attenuation estimates from the TRMM radar. Proc. of Symposium on the Precipitation Observation from Non-Sun Synchronous Orbit, Nagoya, Japan, pp.163-168.

Meneghini, R. and Kozu, T. (1990): Spaceborne Weather Radar. Arctech House, 199pp.

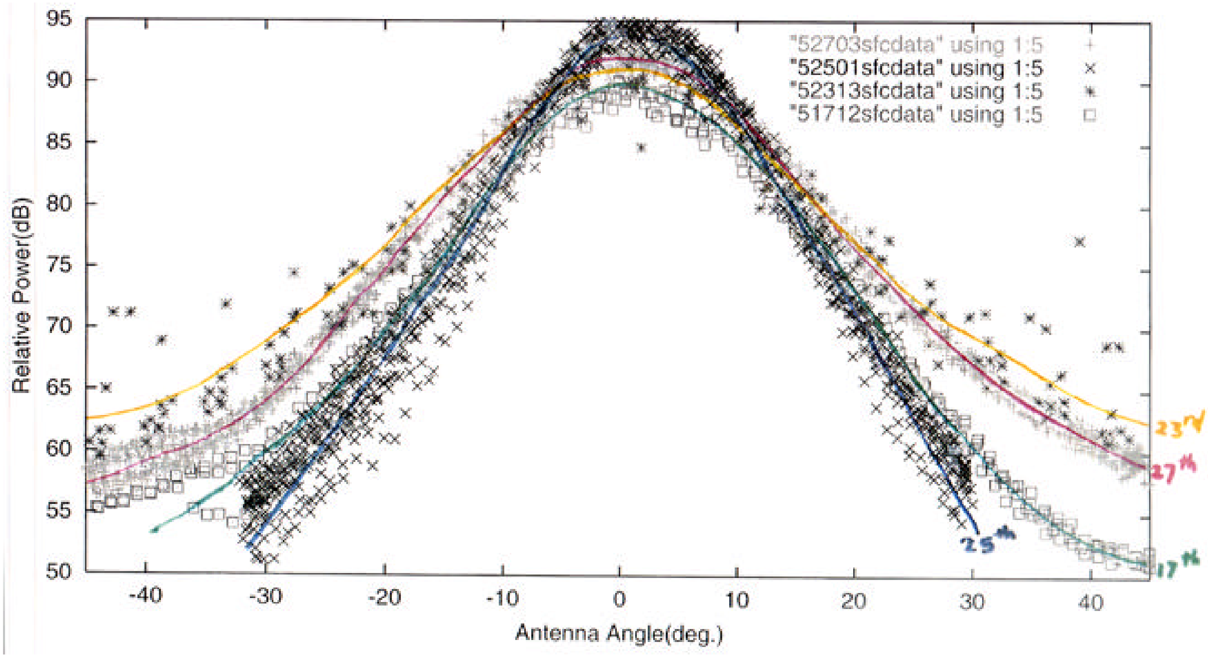

Fig. 2.1 Day-to-day variation in sea-surface characteristics in nearly rain-free areas.

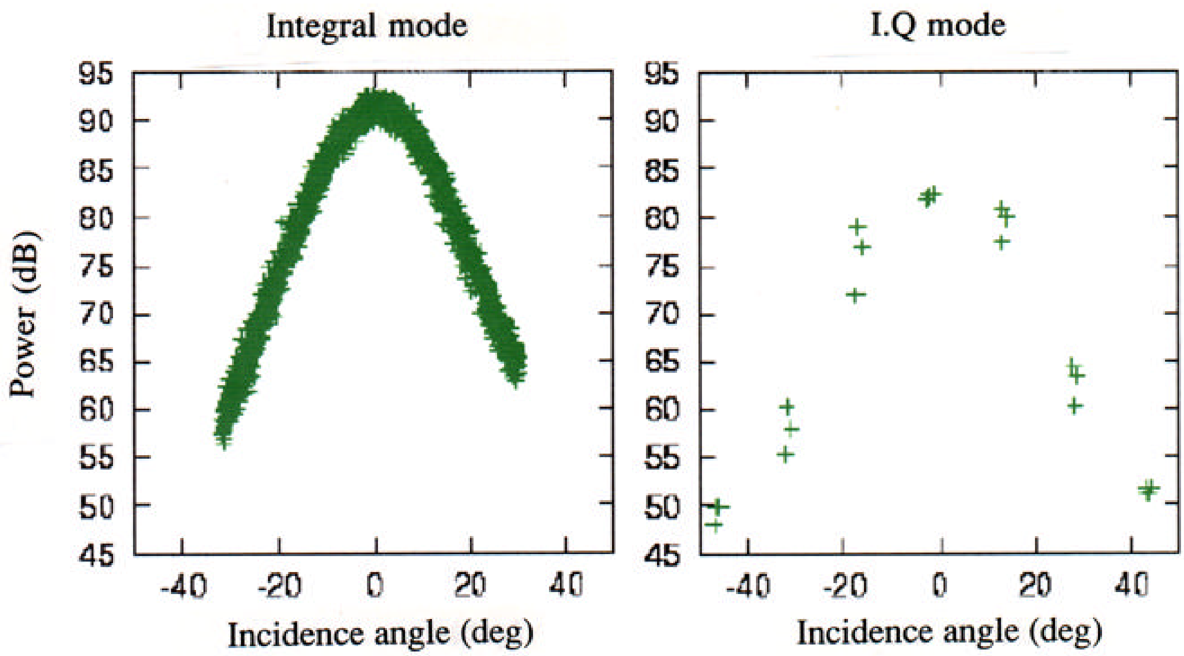

Fig. 2.2 Peak power measured by CAMPR-D; left for Integrated mode and right for I, Q mode. Datasets are immediately adjacent to each other were compared on 26 May 1998.

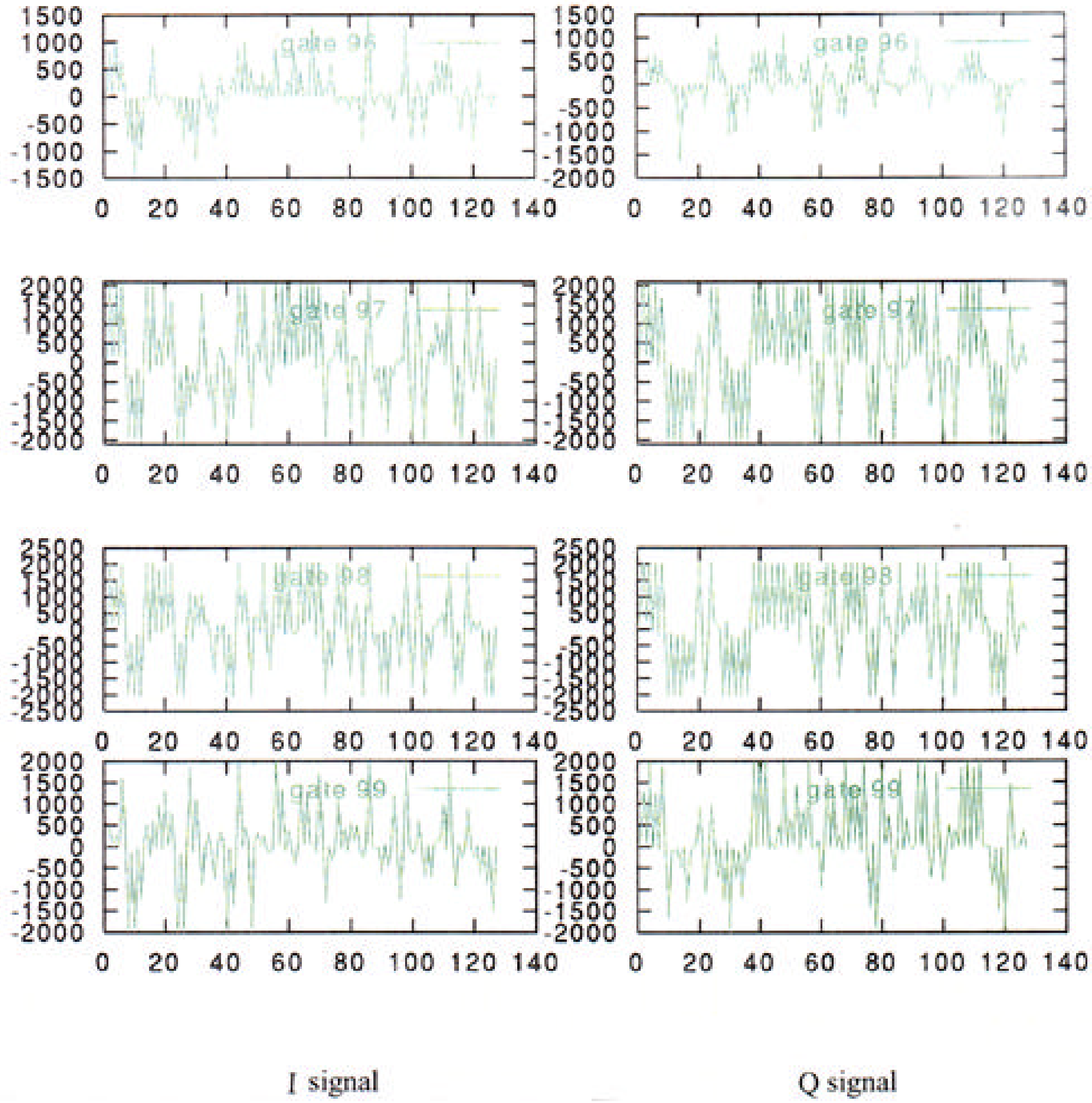

Fig. 2.3 Saturation of I or Q signal at peak surface bin for nadir incidence.

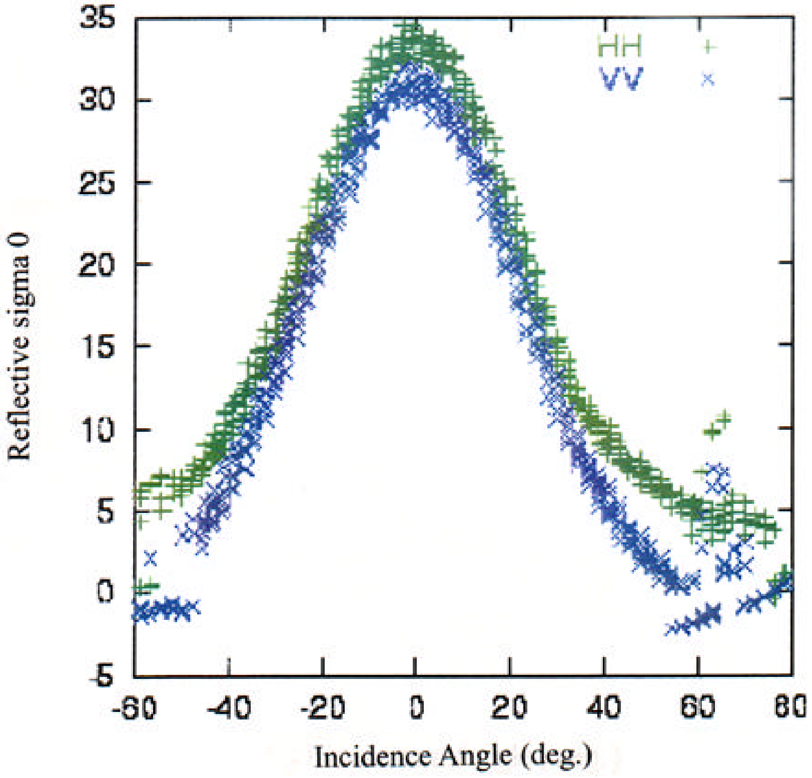

Fig. 2.4 Relative σ_0 measured by CAMPR-D during IMCET.

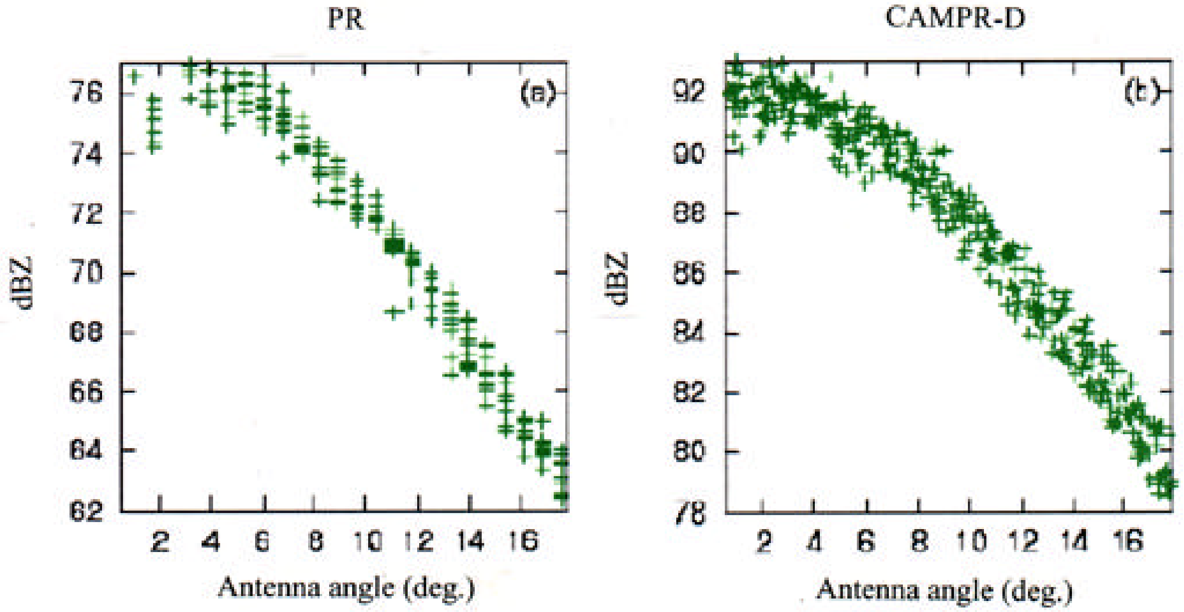

Fig. 2.5 Simultaneous measurements by PR and CAMPR-D.

(a) Peak surface radar reflectivity factor by PR.

(b) Peak surface relative radar reflectivity factor by CAMPR-D on 26 May 1998.

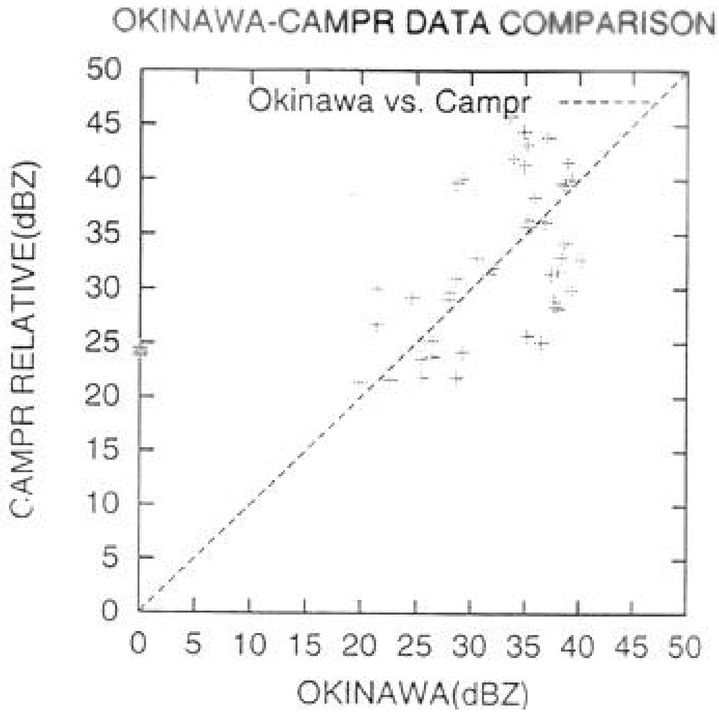

Fig. 2.6 Scatter diagram between Okinawa radar and CAMPR-D on 26 May 1998.

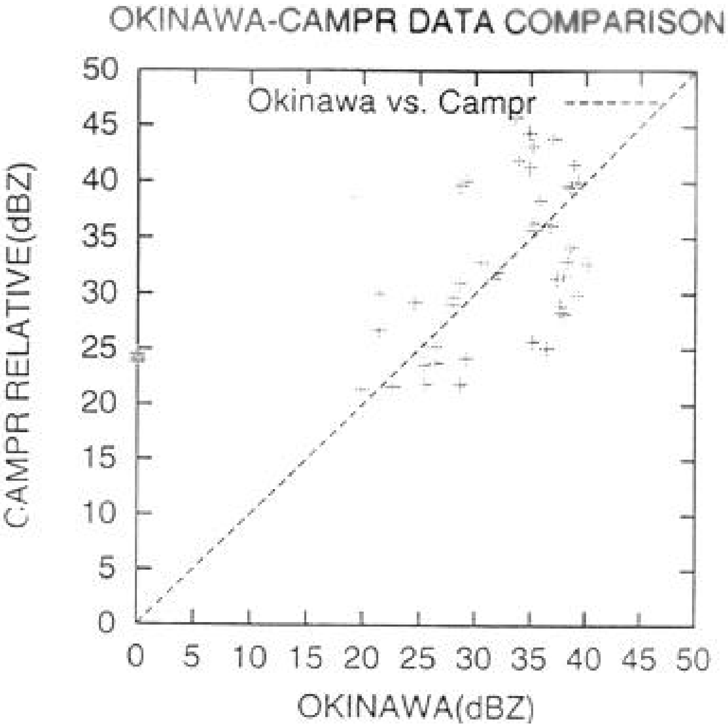

Fig. 2.7 Scatter diagram between Ishigakijima radar and CAMPR-D on 27 May 1998.

3. Comparison of the PR with CAMPR-D

Hiroshi Hanado : Communications Research Laboratory

3.1 Outline of CAMPR-D observation flights

During IMCET ’98, eleven observation flights were conducted and nine simultaneous rain observations with the PR were achieved. Each flight condition is shown in Table 3.1. CAMPR-D observation parameters are summarized in Table 3.2.

Table 3.1 CAMPR-D observation flights during IMCET ’98

CAMPR-D Observation Flight				Simultaneous Rain Observation with the PR			
No.	Date	Objective	Flight Area	Case	TRMM Granule	Time (JST)	Rain Type etc.
1	May 17	radar test flight	Around Nagoya				
2	May 23	Ferry flight #1	From Nagoya to Tanegashima	(i)	2779	11:47	Very weak and Small
3	May 23	Ferry flight #2	From Tanegashima to Miyakojima				
4	May 25	TRMM overpass #1	Around Ishigakijima	(ii)	2811	12:35	Small Area
5	May 26	TRMM overpass #2	Around Okinawa	(iii)	2826	11:23	Large Area Stratiform
6	May 27	TRMM overpass #3	Around Ishigakijima	(iv)	2842	11:46	Convective
7	May 28	TRMM overpass #4	Around Okinawa	(v)	2857	10:34	Very Small Single Cell
8	May 30	TRMM overpass #5	Around Miyakojima	(vi)	2888	9:46	Convective Narrow Rain Band
9	May 31	Simultaneous observation with “MIRAI*”	Around Miyakojima				
10	June 25	TRMM overpass #6	Around Shikoku	(vii)	3303	17:14	Large Area
11	June 26	TRMM overpass #7	Around Nagoya	(viii)	3317	14:25	Small and Weak
				(ix)	3318	16:02	Single Cell

* “MIRAI” is the Japan Marine Science & Technology Center’s Oceanographic Research Vessel which has 3-dimensional doppler radar.

Both CAMPR flight trajectory and the PR rain echo pattern at each TRMM overpass are shown in Figure 3.1. The horizontal distribution of corrected Z factor (2A25) at 1.5 km

Table 3.2 CAMPR-D Observation Parameters at the TRMM Overpass

Case	Date	TRMM granule	CAMPR				
			Mode	Antenna Scanning	Altitude	Data File Name	Time (JST)
(i)	May 23	2779	Polarization	-30 to +30	8164 m	0523_09	11:37:57-11:54:57
(ii)	May 25	2811	Dual Beam	-30 to +30	8666 m	0525_05	12:26:04-12:40:55
(iii)	May 26	2826	Dual Beam	-30 to +30	9148 m	0526_08	11:01:15-11:44:14
(iv)	May 27	2842	Polarization	-20 to +85	9160 m	0527_04	11:36:20-11:51:35
(v)	May 28	2857	Dual Beam	-45 to +45	6245 m	0528_04	10:28:17-10:51:35
(vi)	May 30	2888	Dual Beam	-20 to +85	2908 m	0530_08	09:31:02-09:56:16
(vii)	June 25	3303	Dual Beam	-45 to +45	9509 m	0625_05	17:01:02-17:18:27
(viii)	June 26	3317	Dual Beam	-20 to +85	9213 m	0626_06	14:21:02-14:25:52
(ix)	June26	3318	Dual Beam	-25 to +80	7534 m	0626_15	15:54:25-16:03:51

altitude is displayed with the GMS infrared cloud image. During IMCET’98 (May 23-May30), the weather conditions were not good for simultaneous rainfall observation between the PR and CAMPR-D. At three cases: (i) May 23, (ii) May 25, and (v) May 28, rainfall area was very sparse. In the case (iii) May 26, stratiform rain area was uniformly extended over the East China sea to the west of Okinawa island. At both (iv) May 27 and (vi) May 30 cases, convective rain was observed. During IMCET’98-nagoya (June 25,26), two observation flights were conducted and three simultaneous observations were succeeded. In the case (vii) June 25, large rainfall area was observed over land at the north part of Shikoku. Both (viii) and (ix) June 26 cases were sporadic rain cell.

3.2 Comparison of vertical cross-section

In the Figure 3.2, vertical cross-section of the PR 1C21 uncorrected Z factor (Figure 3.2 (a)) and CAMPR-D received power (Figure 3.2 (b)) are shown. Though the airplane installed CAMPR-D took about 20 minutes to fly along the TRMM track direction, both echo patterns correspond well with each other.

3.3 Comparison of horizontal cross-section

In the Figures 3.3-1, 3.3-2 and 3.4, horizontal cross-section of the PR and CAMPR-D are shown. These images indicate that good correspondence exists between the PR rain echo pattern and that of CAMPR-D. However, the observation area of CAMPR-D is very limited compared with that of the PR, it is not so effective to compare both images directly. Some statistical approach, such as the Contoured Frequency by Altitude Diagrams (CFADs) may be suitable.

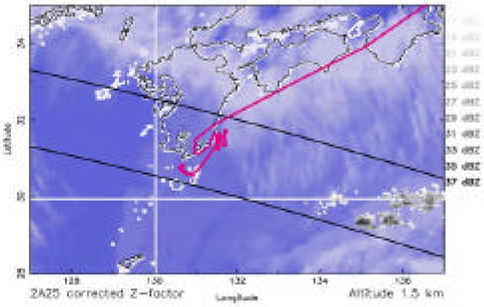

(i). May 23, 1998 02:46:23-02:48:57(UT)

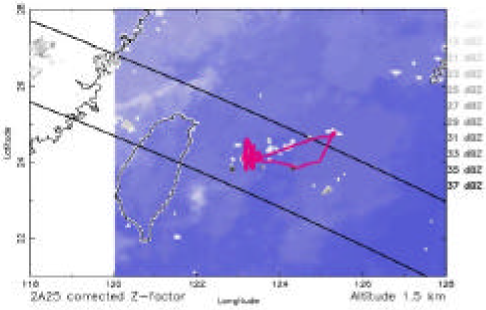

(ii). May 25, 1998 03:33:00-03:35:57(UT)

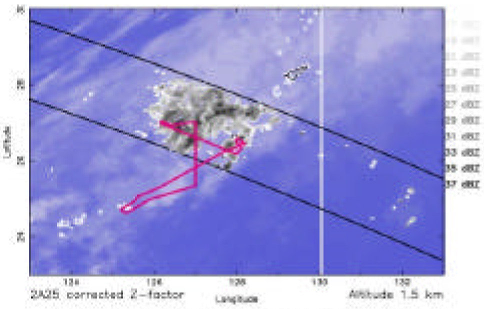

(iii). May 26, 1998 02:21:35-02:24:27(UT)

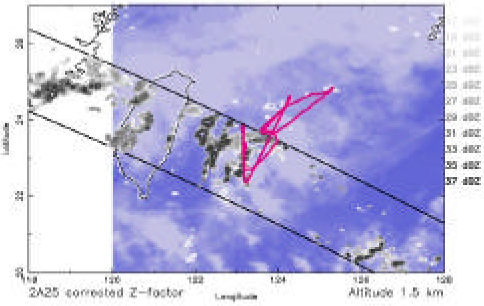

(iv). May 27, 1998 02:44:53-02:47:50(UT)

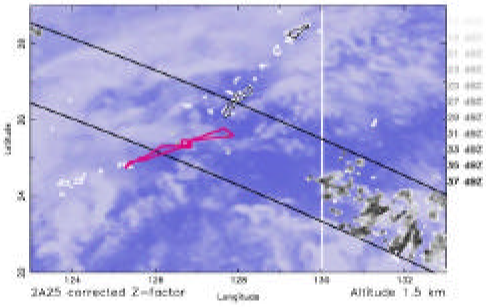

(v). May 28, 1998 01:33:20-01:36:15(UT)

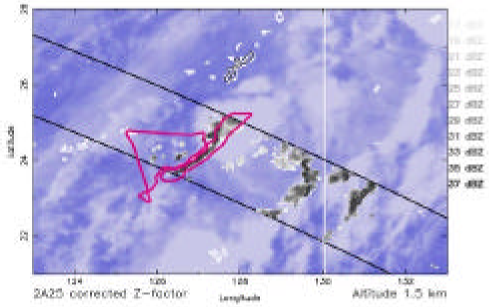

(vi). May 30, 1998 00:44:52-00:47:48(UT)

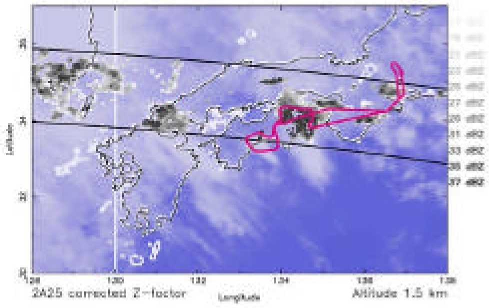

(vii). June 25, 1998 08:12:36-08:14:54(UT)

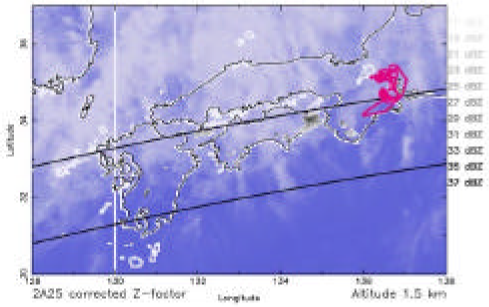

(viii). June 26, 1998 05:23:27-05:25:51(UT)

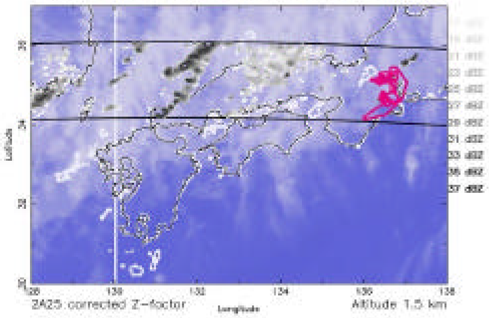

(ix). June 26, 1998 05:23:27-05:25:51(UT)

Figure 3.1

CAMPR flight trajectory and TRMM PR echo pattern at TRMM overpass

(The horizontal distribution of corrected Z factor (2A25) at 1.5 km altitude is displayed with the GMS infrared cloud image.)

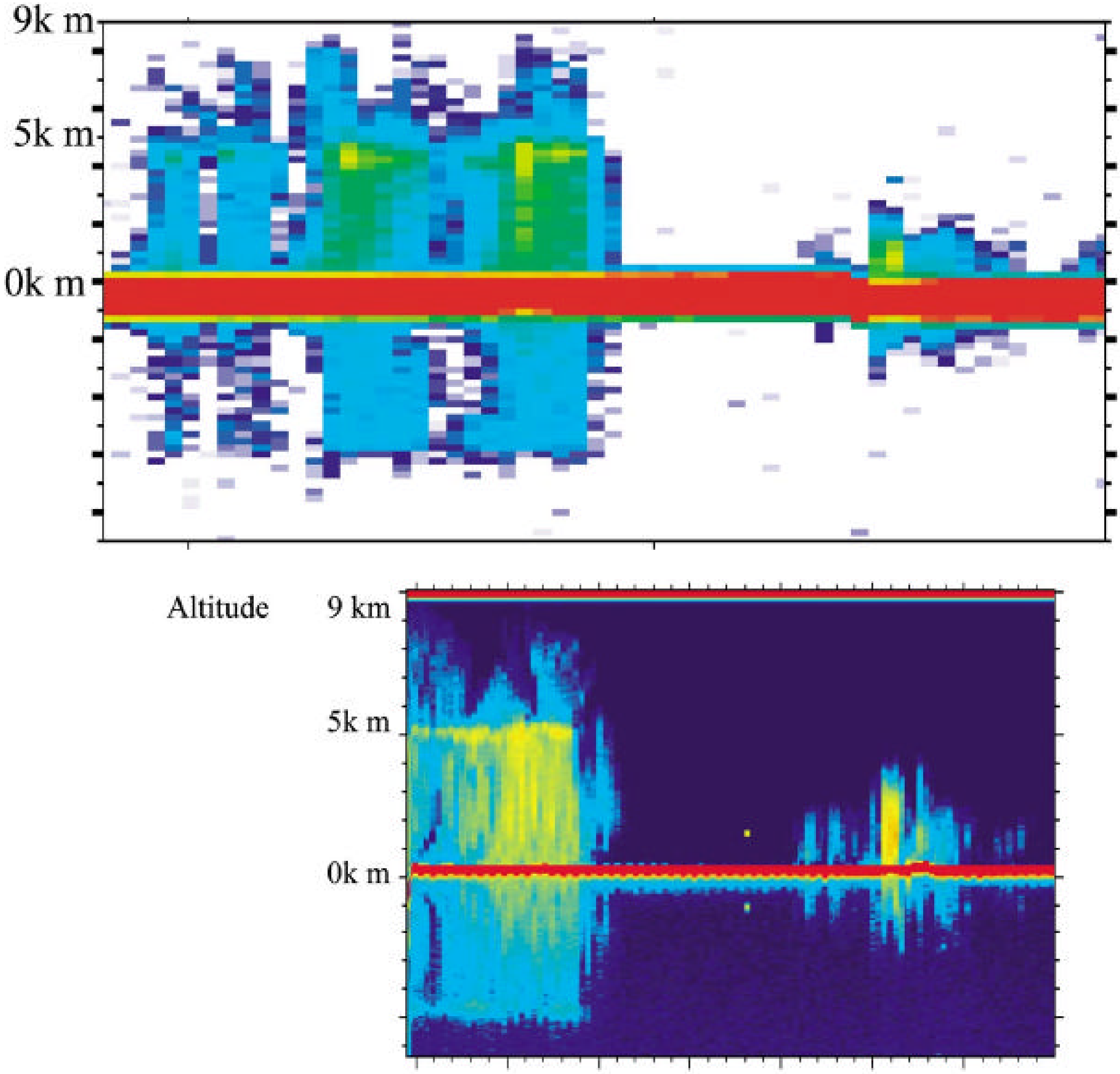

(a). TRMM PR 1C21 uncorrected Z factor

(b). CAMPR-D Received Power

Figure 3.2 Vertical cross-section of TRMM PR 1C21 uncorrected Z factor and CAMPR-D received Power
(iii) May 26, 1998 TRMM granule 2826
CAMPR 0526_08

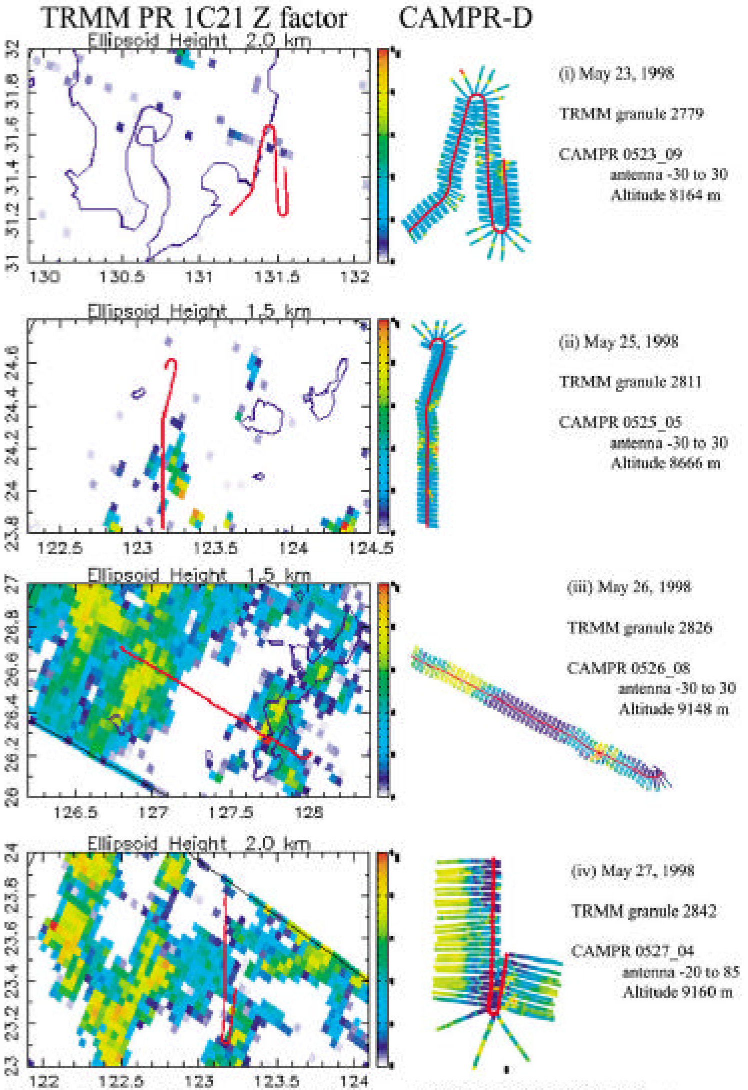

(i) May 23, 1998

TRMM granule 2779

CAMPR 0523_09
antenna -30 to 30
Altitude 8164 m

(ii) May 25, 1998

TRMM granule 2811

CAMPR 0525_05
antenna -30 to 30
Altitude 8666 m

(iii) May 26, 1998

TRMM granule 2826

CAMPR 0526_08
antenna -30 to 30
Altitude 9148 m

(iv) May 27, 1998

TRMM granule 2842

CAMPR 0527_04
antenna -20 to 85
Altitude 9160 m

Figure 3.3-1 Horizontal Distribution of TRMM PR 1C21 Z factror and CAMPR Received Power

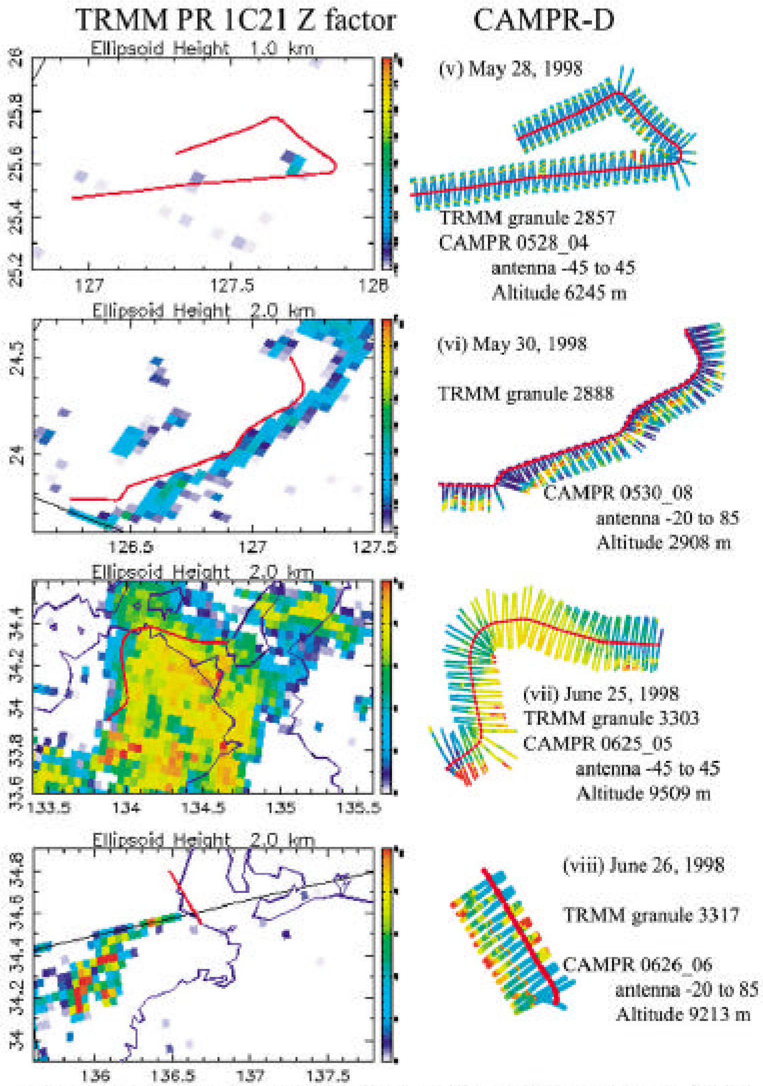

(v) May 28, 1998

TRMM granule 2857
CAMPR 0528_04
antenna -45 to 45
Altitude 6245 m

(vi) May 30, 1998

TRMM granule 2888

CAMPR 0530_08
antenna -20 to 85
Altitude 2908 m

(vii) June 25, 1998
TRMM granule 3303
CAMPR 0625_05
antenna -45 to 45
Altitude 9509 m

(viii) June 26, 1998

TRMM granule 3317

CAMPR 0626_06
antenna -20 to 85
Altitude 9213 m

Figure 3.3-2 Horizontal Distribution of TRMM PR 1C21 Z factor and CAMPR Received Power (a). TRMM PR 1C21 Z (dBZ)

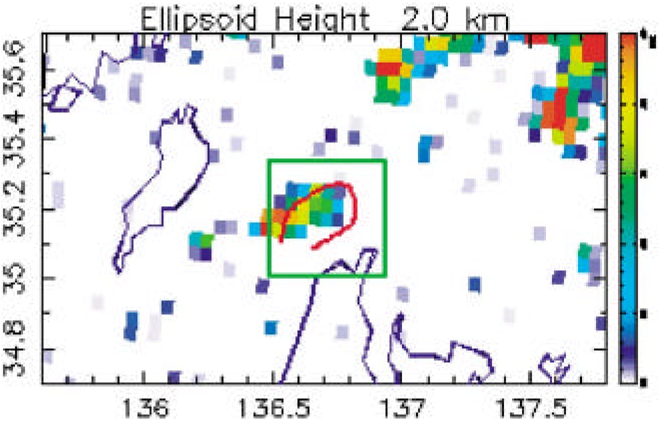

(b). CAMPR-D Received Power (averaged)

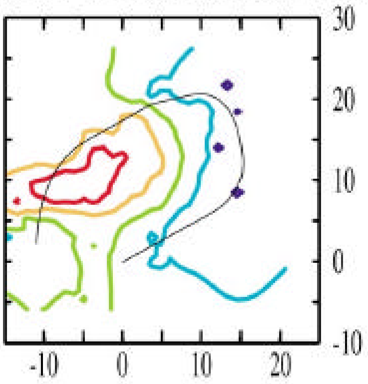

(c). CAMPR-D Received Power

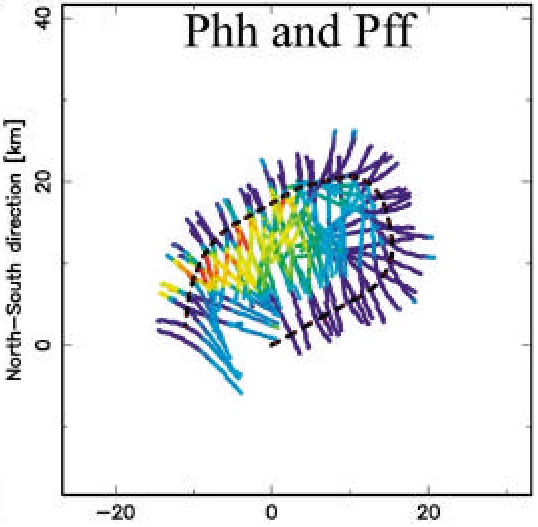

CAMPR 0626_15
antenna -25 to 80
Altitude 7534 m

Figure 3.4
Comparison between TRMM PR uncorrected Z factor and CAMPR-D Received Power at 2.0 km altitude
(ix) June 26, 1998 TRMM granule 3318

4. Comparison of the PR with Ground-based Radar

Kinji Furukawa : National Space Development Agency of Japan

4.1 Simultaneous observations by the PR and ground-based radars

The radar reflectivity observed by the PR should be validated by comparison with ground observations. In the Ishigaki/Miyako Campaign Experiment for TRMM (IMCET), the Japan Meteorological Agency’s (JMA's) two ground-based radars (Okinawa and Ishigakijima) succeeded in making several simultaneous observations with the PR. This section seeks to validate the PR data using these ground data.

The TRMM orbit with the PR swath width, the CAMPR-D (see the section 3) trajectory, and the coverage of the Okinawa and Ishigakijima radars within a radius of about 100 km diameter for May 26, 1998 are shown in Figure 4.1. In this case, there was a large rain area northwest of Okinawa. The PR observed the overlapping area with the Okinawa radar at around 11:23 Japan Standard Time (JST). The attenuation-corrected radar reflectivity factor (Ze) at 2.5 km height obtained around 11:23 a.m. (JST) by the PR is shown in Figure 4.2 (a), and the Z factor observed by the Okinawa radar is shown in Figure 4.2 (b). On May 30, 1998 at 03:18 a.m., the PR and the Ishigakijima radar observed overlapping areas. At that time, there was an expanding precipitation system south of Ishigakijima. Figure 4.3 (a) shows the distribution of radar reflectivity observed by the PR, and (b) shows that observed by the Ishigakijima radar. In these two cases, though there are some differences in absolute value of the Z factor, the horizontal distribution is apparently quite similar. Other data observed in IMCET’98 are presented in the section 6.

4.2 Comparison results between the PR and the ground-based radar

The horizontal distribution is apparently quite similar in the two simultaneous observations by the PR and ground-based radars. However, there are some differences in the absolute value of the Z factor, so we have to consider the reasons for the discrepancies.

First, the ground-based radar observes only a few elevations, so the data at a fixed height seem like concentric circles centered on the ground-based radar (Figure 4.4). In Figures 4.2 (b) and 4.3 (b), the gap is filled by the lower height data for the rain pattern comparison. In these cases, we assumed there were no drastic changes in the vertical structure of the rain, so the error caused by the vertical structure change which we can see in the CAMPR-D data (see the section 3) is included. Furthermore, the ground-based radar takes about 7.5 minutes for 1 volume scan, but the PR observes the same area in only a few seconds. The error caused by this absolute time difference is included, too.

Considering these errors, we tried to perform a quantitative comparison. To exclude errors from the vertical structure of the rain, we used only the concentric circle data as the ground-based radar data to make scatter diagrams. Because of the difference of the direction of observation, the rain attenuation is different, so we use the attenuation-corrected radar reflectivity factor (Ze) as the PR data in the level 2 product. It is difficult to estimate the effect of the attenuation from the rain for ground-based radar data. In this case, the rain was not so heavy as to cause drastic attenuation, so we used the raw data for this comparison.

Considering the time and space differences, we averaged radar reflectivity in 10 km by 10 km boxes. Using these data, we plotted scatter diagrams of radar reflectivity for the PR and the ground-based radars. Figure 4.5 is a scatter diagram of the radar reflectivity for the PR and Okinawa radar for the case indicated in Figure 4.2. Figure 4.6 is the scatter diagram for the PR and Ishigakijima radar shown in Figure 4.3. Roughly speaking, the PR and the ground-based radars agree well in both cases, though there is an obvious bias in the Okinawa radar's data. The Okinawa radar tends to detect a larger radar reflectivity than the PR. Also, the regression line deviates from an inclination of 45 degrees. Other results from the data observed in IMCET'98 are presented in the section 6. In these cases, it is difficult to quantitatively validate the PR data by one-to-one comparison of 10km averaged data which has large variances. This disagreement is caused by the absolute time difference of two observations, the effect of the data processing filters applied in JMA's radars to eliminate the interference, and so on. For the absolute observing time difference, we should use only one elevation scan or one azimuth scan close to the PR observation time. However, we didn't adopt this way in this section. For the effect of the filters, we should consider calibrating the radar and estimating the effect of the filters. For these purposes, we conducted an engineering check of the Ishigakijima radar jointly with JMA. As a result, we found that Ishigakijima radar appears to be fairly well calibrated within 1dB without filters. The data processing filters applied in JMA radars are the Moving Target Indicator (MTI) filter, the two-pictures comparing filter, and the sweep comparing filter. To estimate the effect of these filters, we observed rain in the "on" and "off" state of each filter. These experimental observations revealed the apparent effects of the filters. For example, Figure 4.7 (a) shows the rain echo with the MTI filter "on," and (b) shows the rain echo with "off." We can see some differences in both data, but these differences might change for each precipitation system. It is thus difficult to estimate the absolute value of the effect of the filters.

We should compare the averaged value of data including these errors because we can not separate these errors from true value. This analysis demonstrated that the Ishigakijima radar detects about a 0.13 dBZ larger value than the PR and that the Okinawa radar detects about a 2.67 dBZ larger value than the PR. Considering that the PR is calibrated to about 1 dB and has stable performance, we can conclude that the Okinawa radar detects about 2.54 dBZ lager value than the Ishigakijima radar including the effects of filters. This result is consistent with the fact that the Okinawa radar detects a larger value than the Ishigakijima radar in the overlapping area of the two radars.

The purpose of this analysis is to validate the PR data using ground-based radar data, but the result shows that we can compare two separated ground-based radars using the PR. This means that we can use the PR as the "space calibrator" for ground-based radars. This will be the another way of using the PR data.

In this section, we showed some comparison results between the PR and the ground-based radar using the data observed in the Ishigaki/Miyako campaign experiment for TRMM. The rain pattern observed by the PR and the ground-based radar agreed well. However we concluded that it is difficult to validate the PR data quantitatively using JMA's ground-based radar data. For this purpose, we should use a well-calibrated high-resolution ground-based radar without data processing filters. We further concluded that the PR data can be used as a "space calibrator" for separated ground-based radars. This will be another way of using the PR data.

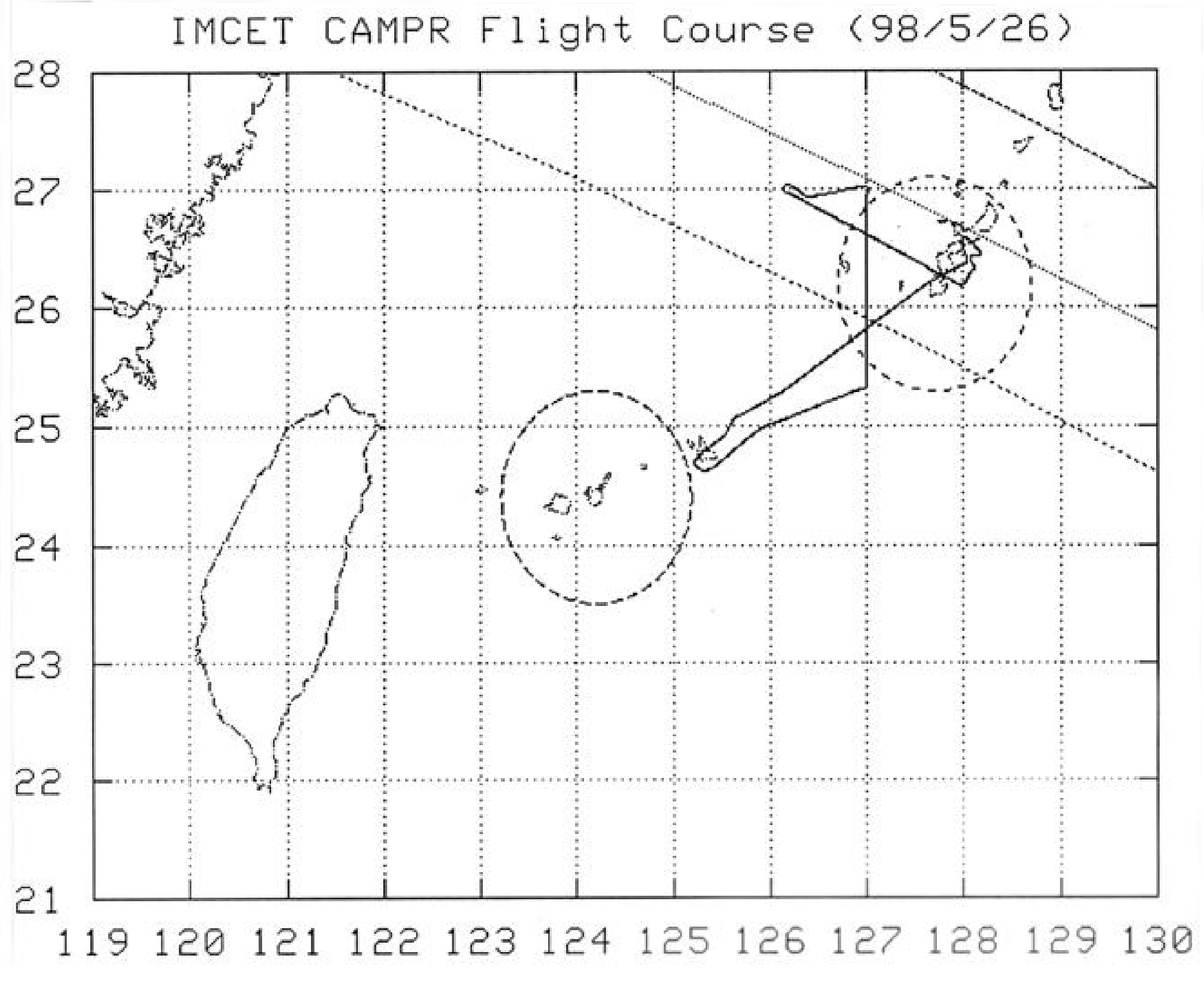

Fig. 4.1 Trajectory of the airborne radar (CAMPR-D) and the coverage of Okinawa weather radar (upper right) and Ishigakijima radar (near center) operated by JMA.

(a) PR2A25 1123JST 26MAY1998 (Lev=2.5km)

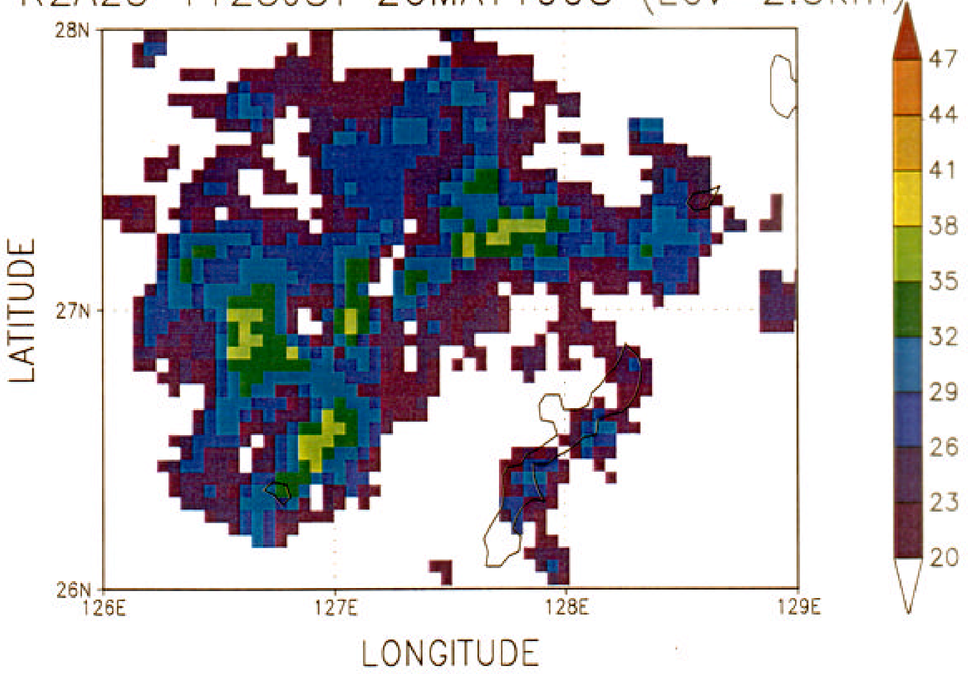

(b) OKINAWA 1122JST 26MAY1998 (Lev=2.5km)

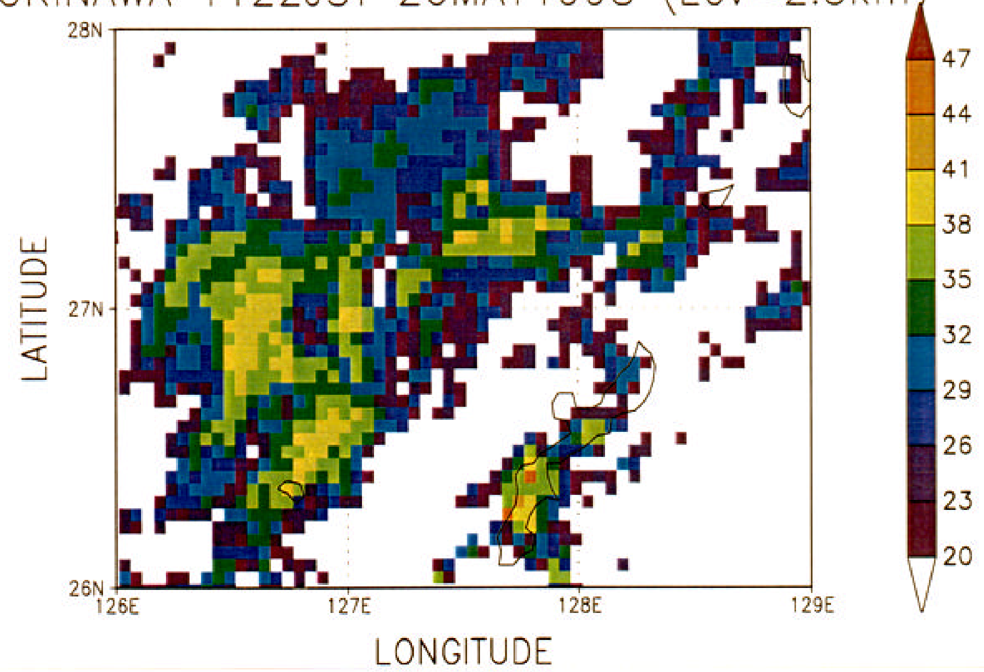

Fig. 4.2 Horizontal pattern of radar reflectivity (attenuation corrected) by the PR (a) and Okinawa ground based radar (b) at 2.5km height taken almost at the same time.

(a) PR2A25 0318JST 30MAY1998 (Lev=2.5km)

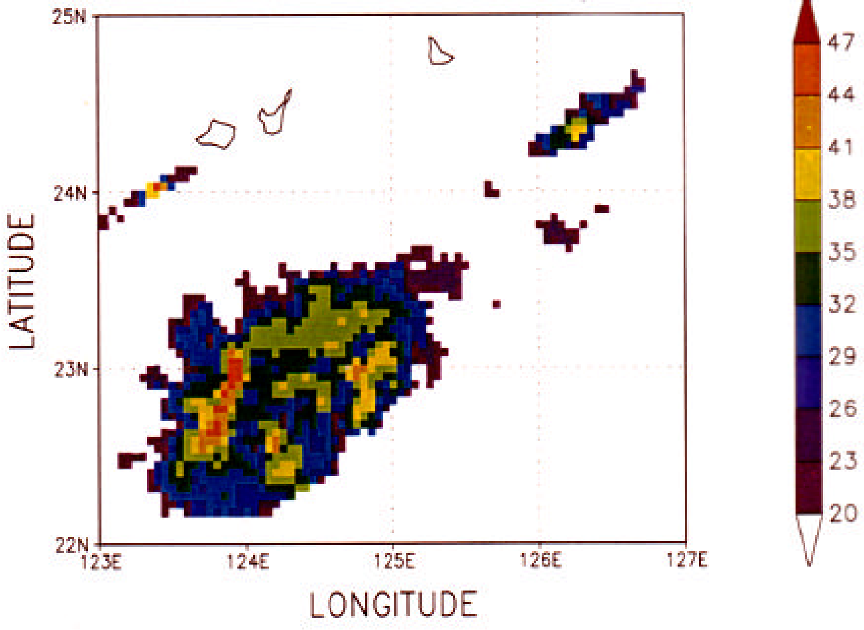

(b) ISHIGAKI 0314JST 30MAY1998 (Lev=2.5km)

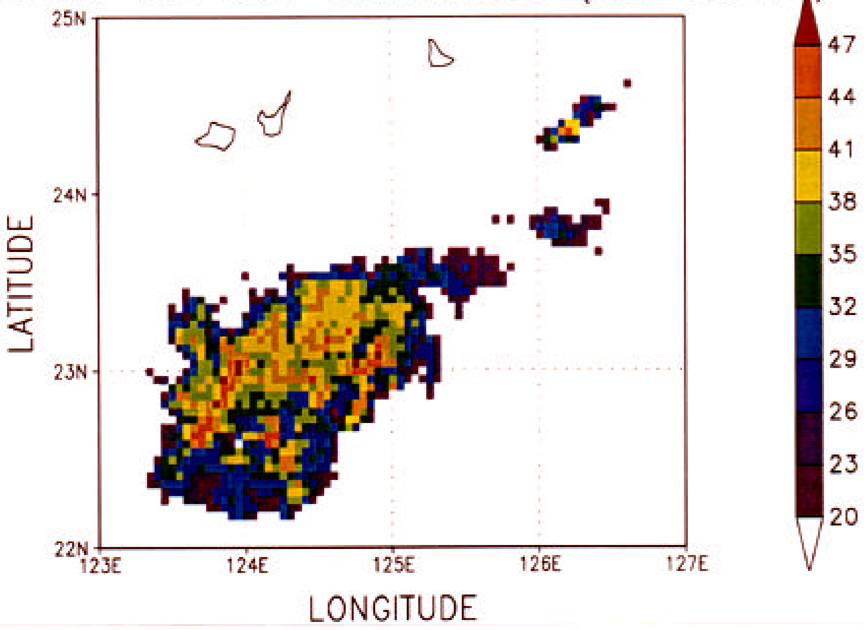

Fig. 4.3 Horizontal pattern of radar reflectivity (attenuation corrected) by the PR (a) and Ishigakijima ground based radar (b) at 2.5km height.

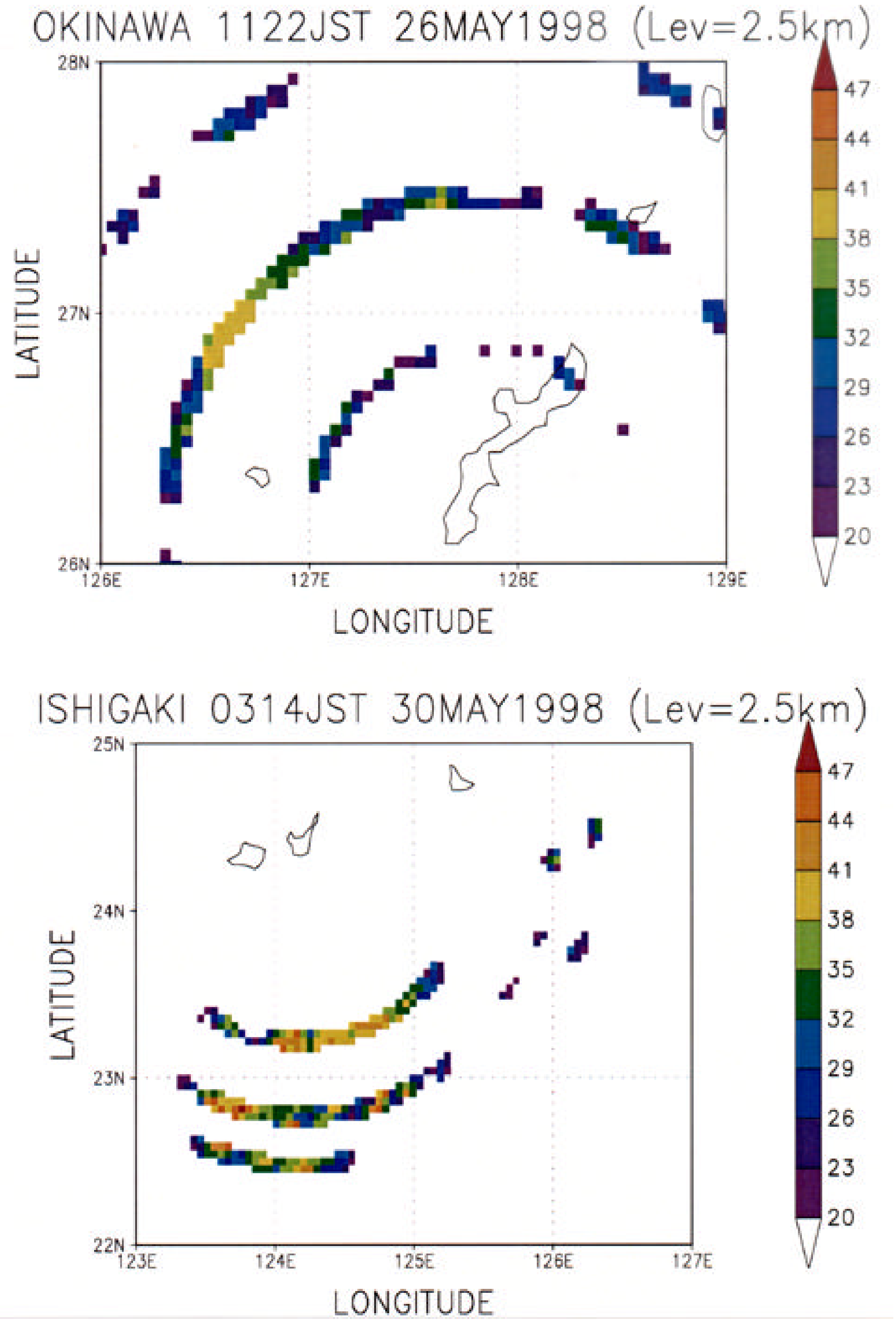

Fig. 4.4 The ground-based radar data at a fixed height. This seems like concentric circles centered on the ground-based radar.

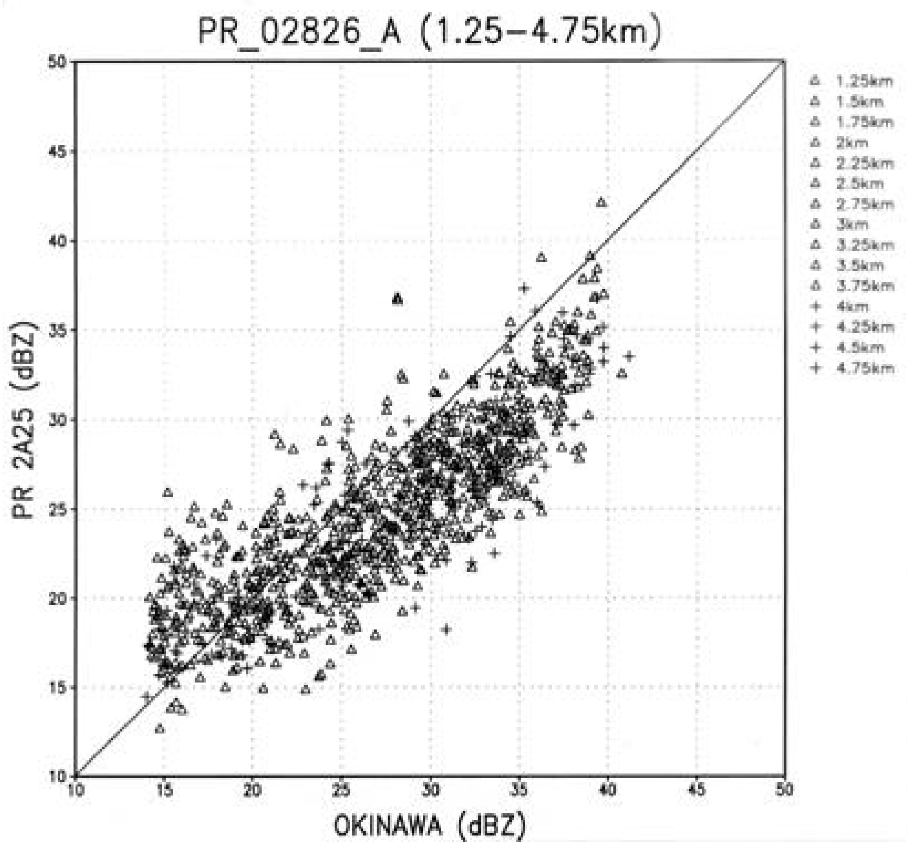

Fig. 4.5 The scatter diagram of the radar reflectivity for the PR and Okinawa radar for the case indicated in the Fig. 4.2.

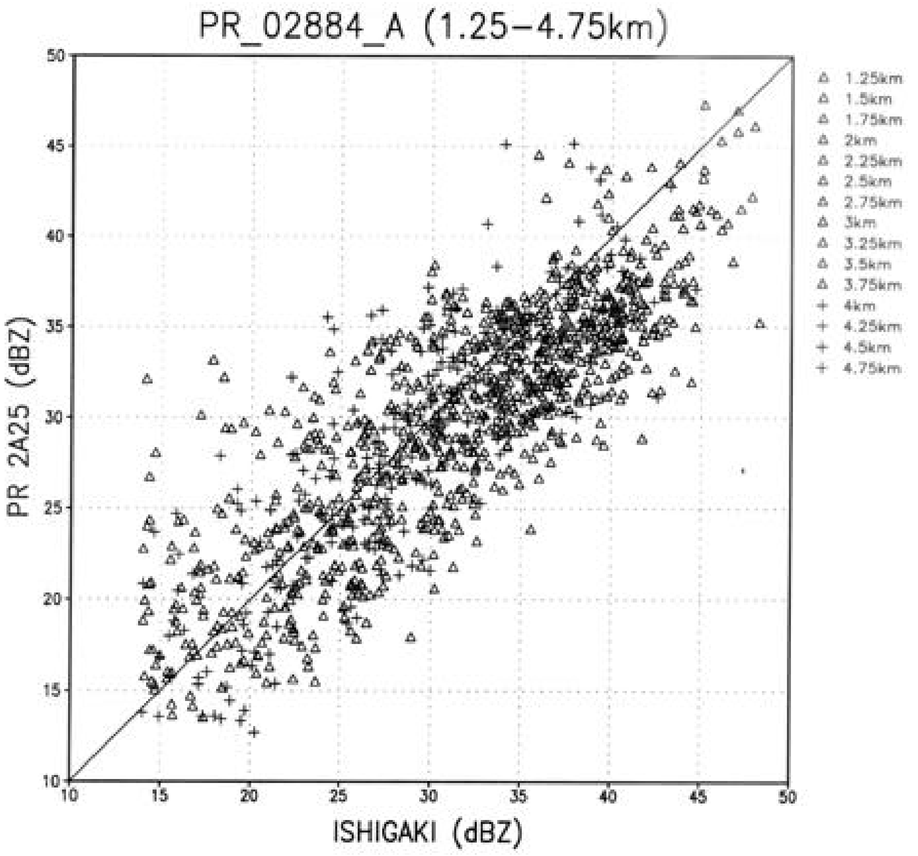

Fig. 4.6 The scatter diagram of the radar reflectivity for the PR and Ishigakijima radar for the case indicated in the Fig. 4.3.

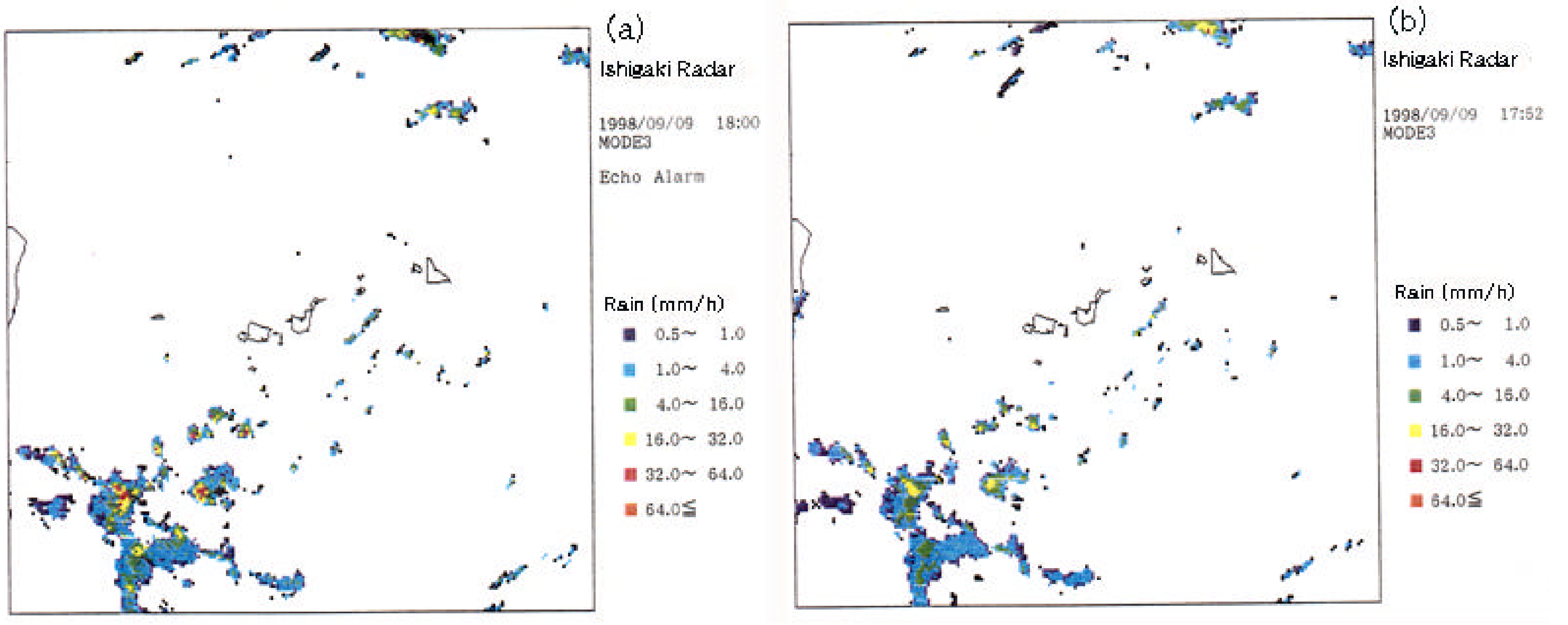

Fig. 4.7 The rain echo observed by Ishigakijima radar with the MTI filter “on” (a) and “off” (b).

5. Sonde Operation

Kenji Nakamura : Nagoya University

At the IMCET period, enhanced sonde operation by JMA was performed. This enhanced sonde operation was a part of activity of the GEWEX Asian Monsoon Experiment (GAME). Using the sonde data set, we tried to get apparent sensible and latent heat budget. Figure 5.1 shows the sonde operation sites related to IMCET with a PR swath on 26 May. We had 4 sites: Naze, Okinawa, Keifumaru (JMA’s meteorological observation vessel) and Ishigakijima.

The analyzed period was from 22 May to 31 May. Figure 5.2 shows the zonal and meridional wind velocity for Region B during this period. Sonde data for three sites surrounding Region B are averaged. North-Easterly wind was dominant before 25 May, followed by South-Westerly wind. Figures 5.3 and 5.4 are the temperature and the specific humidity. After 25 May, lower atmosphere was more humid.

Using three sonde soundings, we calculated the budget for each triangle (A and B). Figure 5.5 shows the basic formula for the calculation of the diabatic heating using sonde observations. We sliced the atmosphere into layers of about 20 hPa from near surface (about 1,000 hPa) to up to about 100 hPa. The most erroneous one is the up/down draft estimation using continuity equation. We tried to set zero at the lowest level or at the top (usually about 100 hPa where sonde data is available). Since the former did not give reasonable result, we mainly used the latter condition. We also tried a linear combination of them. Figure 5.6 shows the result of Q1 and Q2 for each region. Region C is a triangle one with Minami-Daitojima, Okinawa and Naze).

Estimation of the profile of latent heat release is one of the targets of TRMM. A very simple algorithm for the estimation is to have a vertical derivative of the rainrate measured by the PR. The rainrate is vertical water flux. If all the water condensed from water vapor becomes precipitation. The vertical derivative of the rainrate become the amount of the condensation if lateral flux is negligible. The lateral flux may be neglected when we take sufficiently large area, in other words, make the lateral boundary has no precipitation or cloud. The averaged Q1 and Q2 over the period for each region (A, B and C) are shown Figure 5.7.

Figure 5.8 is the PR observation for 24 to 28 May. We had only five overpasses during that period. The precipitation type were mainly stratiform as shown in Figure 5.9. The storm heights were more than 6 km on 26, 27 and 28 May as shown in Figures 5.10 and 5.11. The bright band height and the freezing levels were about 5 km, which is a typical one during this season (Figures 5.12 and 5.13).

Figures 5.14 (a)-(d) show the vertical rain structure, etc. averaged over the area (A), (B) or (C). The vertical derivatives are also shown. Since the profile of rainrate shows the bright band, the vertical derivatives show a positive peak just above the bright band, and a negative peak just below the bright band. Though the PR algorithm uses a Z-R relationship for the melting layer, the bright band is still apparent. This suggests that the PR algorithm should take care of the bright band more precisely. The bright band is also appeared in Figure 5.11, which shows the vertical cross section of precipitation observed by the PR.

As a summary, the vertical derivative of the precipitation estimated by the PR has some similarity with the estimation from radio sonde data. There, however, exist many discrepancies. Once is due to up/down draft estimate from sonde data. Generally speaking, the rain case we analyses was not so heavy one and the estimation from sonde data has inevitably much errors. Rain rate estimation at bright band is also an error cause.

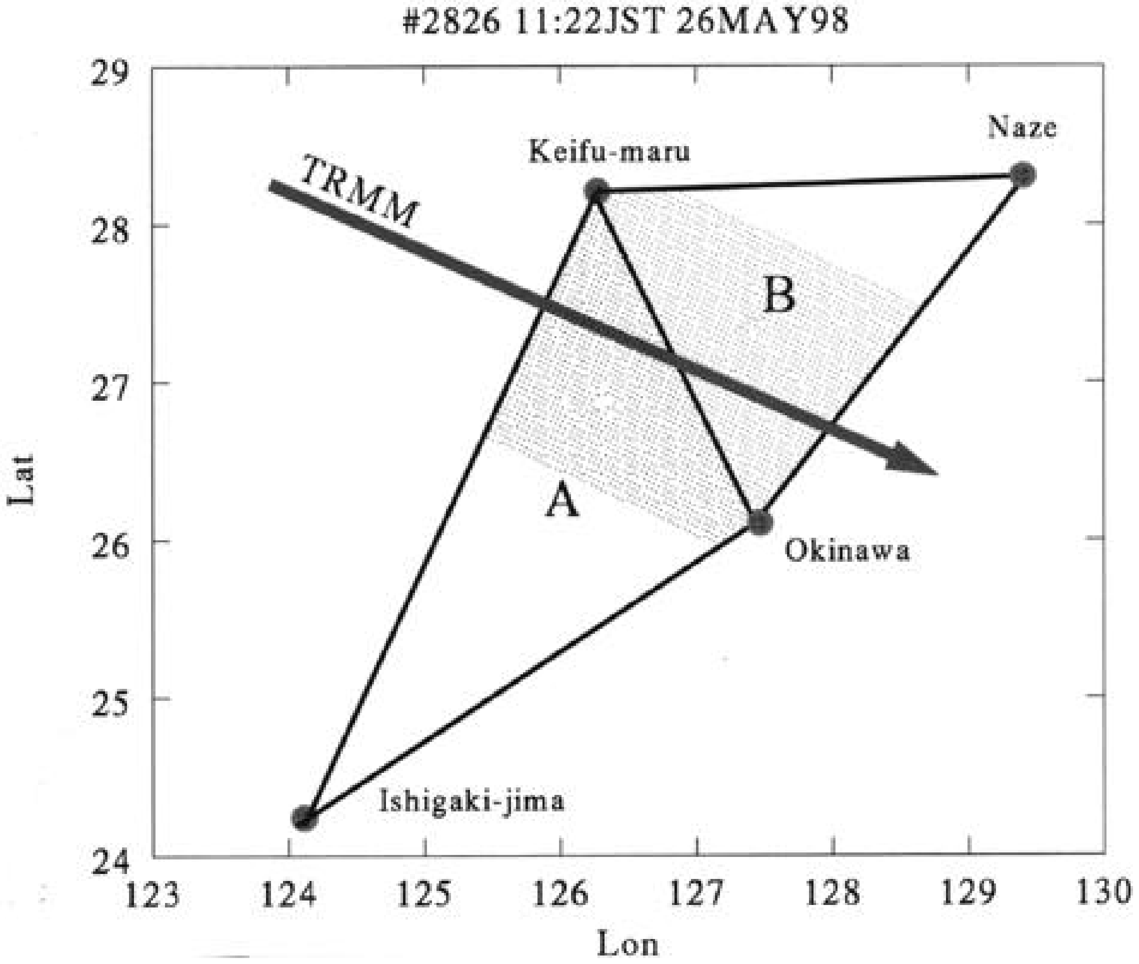

Fig. 5.1 Sonde operation sites related to IMCET with a PR swath on 26 May.

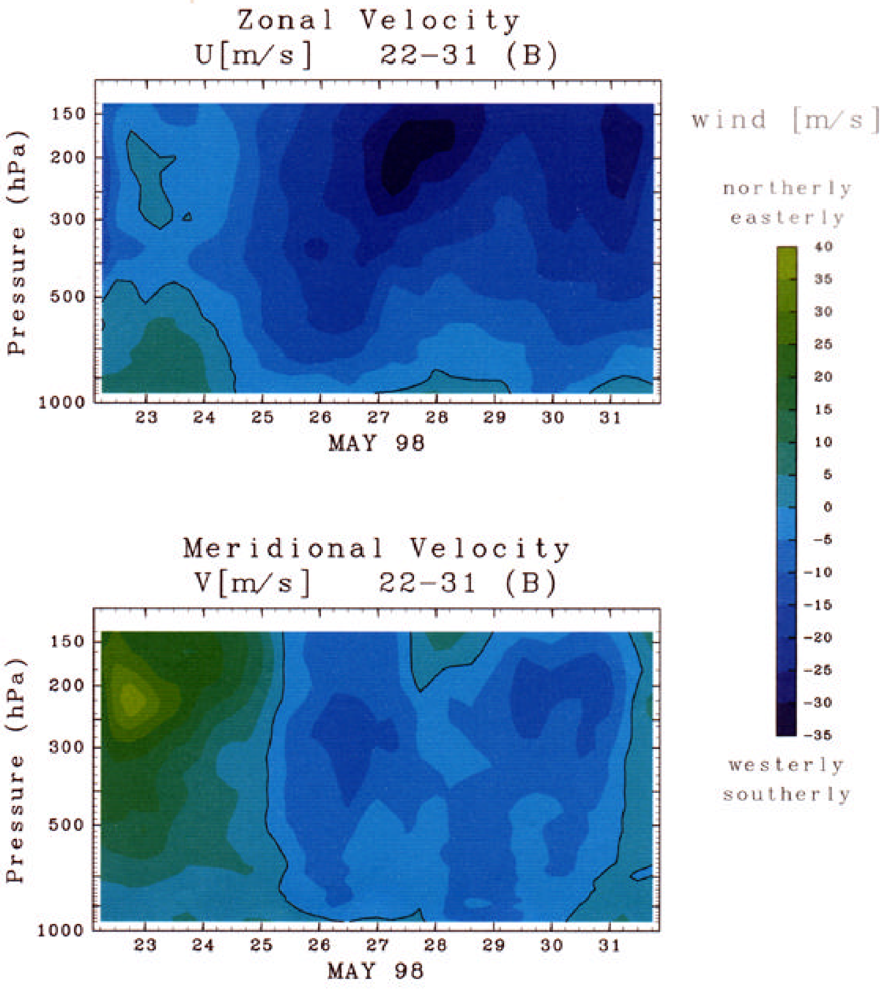

Fig. 5.2 Zonal and meridional wind velocity for Region B from 22 May to 31 May.

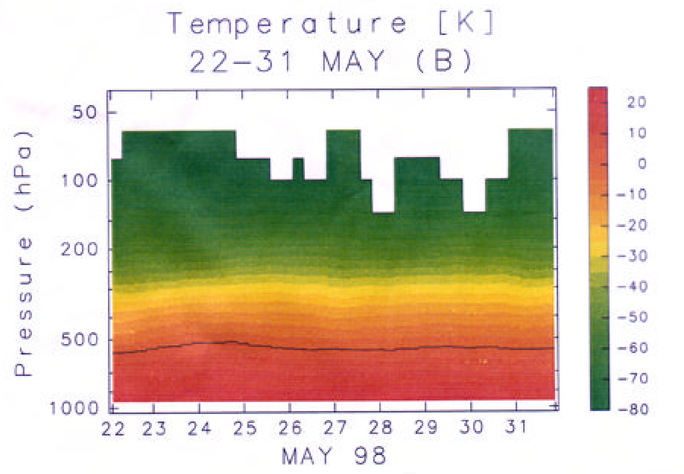

Fig. 5.3 Temperature for Region B from 22 May to 31 May.

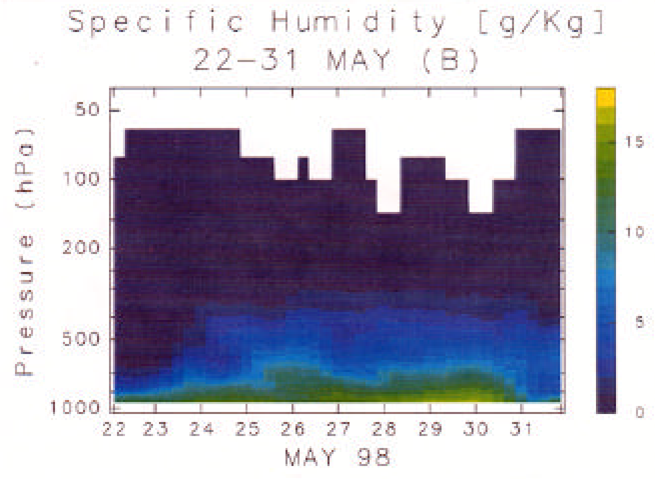

Fig. 5.4 Specific humidity for Region B from 22 May to 31 May

$$\text{moist static energy} \quad h = \overbrace{gz + C_pT}^{\text{dry static energy}} + \underbrace{Lq}_{\text{latent heat energy}} \qquad (1)$$

The heat and moisture equations become, viz.

$$Q_1 \equiv \frac{\partial \bar{s}}{\partial t} + \nabla \cdot \overline{sv} + \frac{\partial \overline{s\omega}}{\partial p} = Q_R + L(\overline{C} - \overline{e}) - \frac{\partial \overline{(s'\omega')}}{\partial p}, \qquad (2)$$

$$Q_2 \equiv -L\left(\frac{\partial \bar{q}}{\partial t} + \nabla \cdot \overline{qv} + \frac{\partial \overline{q\omega}}{\partial p}\right) = L(\overline{C} - \overline{e}) + L\frac{\partial \overline{(q'\omega')}}{\partial p} \qquad (3)$$

where Q_1(apparent heat sources), Q_2(apparent moisture sinks).

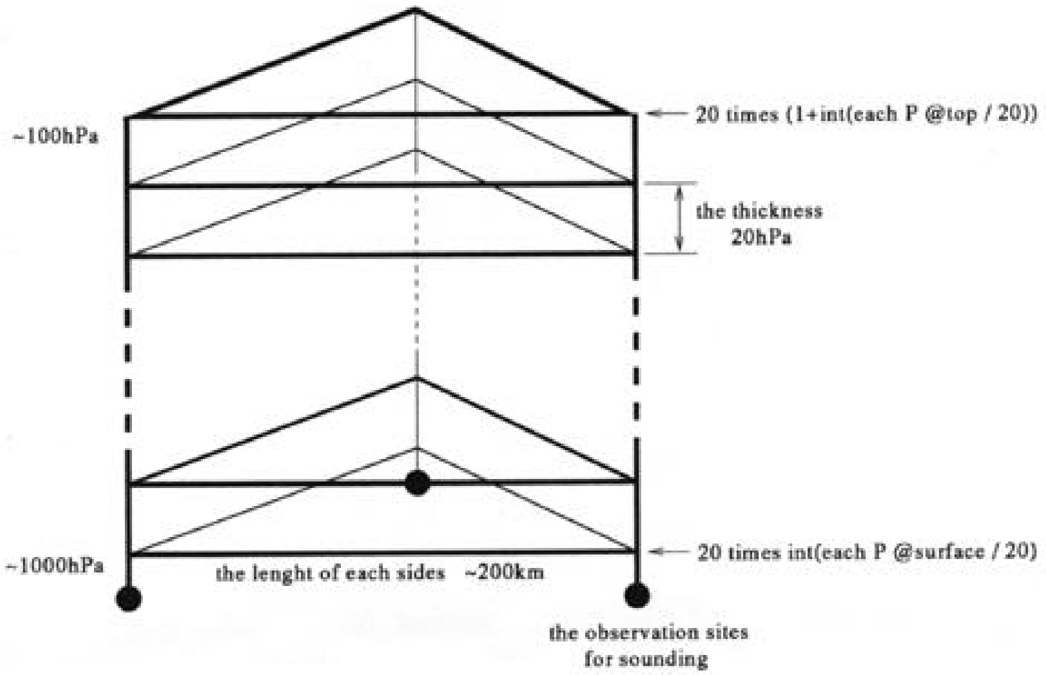

Fig. 5.5 The basic formula for the calculation of the diabatic heating using sonde observations.

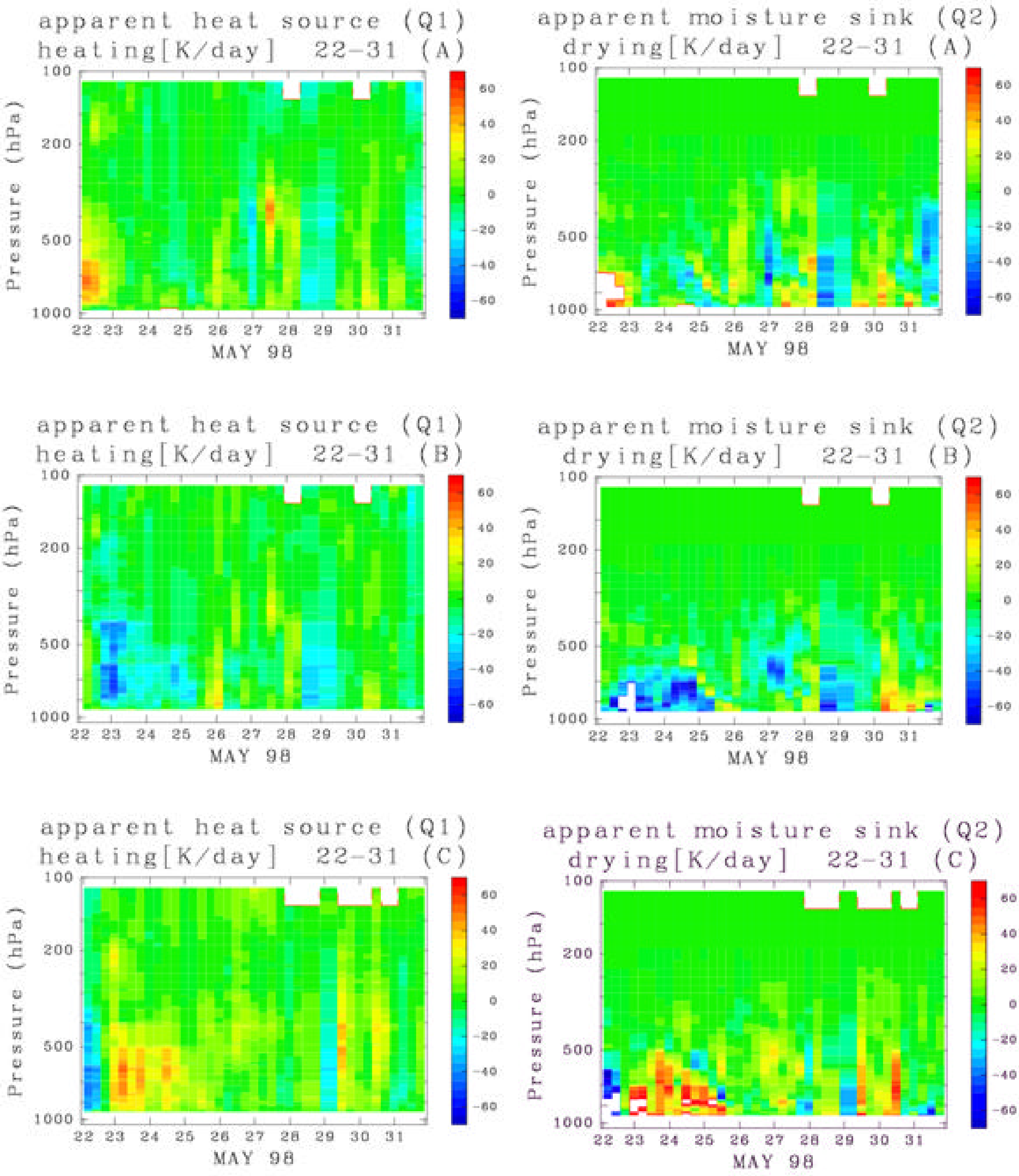

Fig. 5.6 The results of Q1 and Q2 for region A (upper), B (middle) and C (bottom).

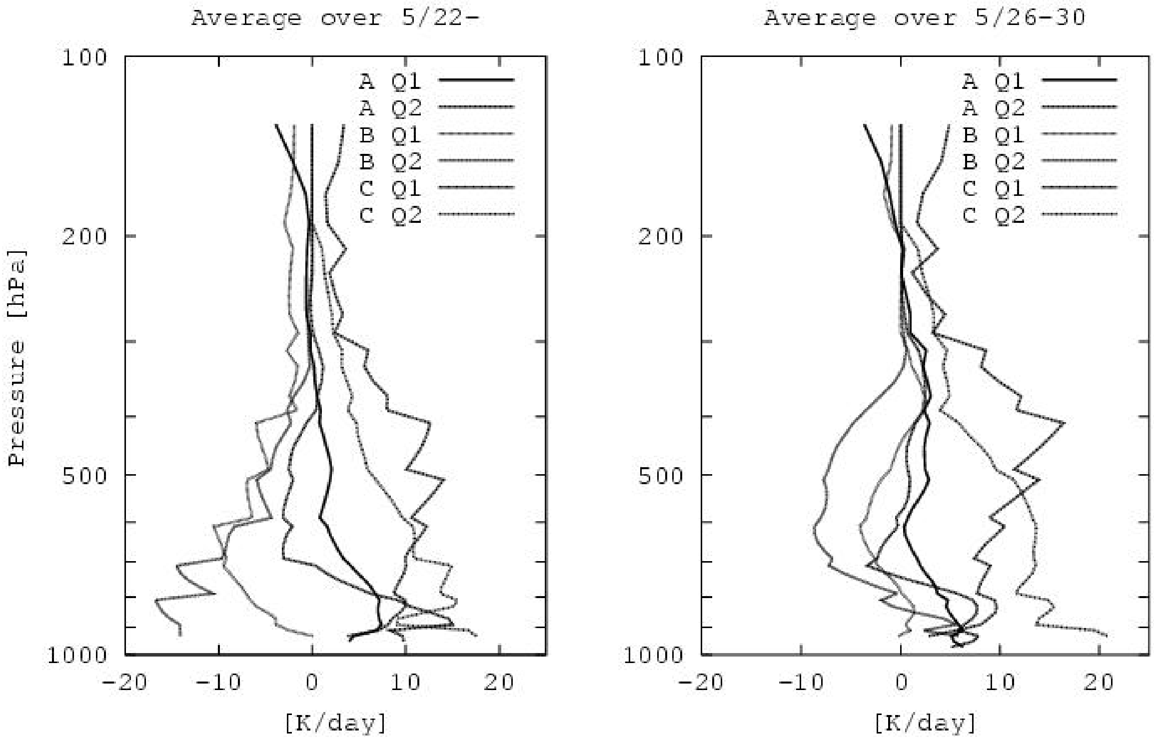

Fig. 5.7 The averaged Q1 and Q2 over the period for each region

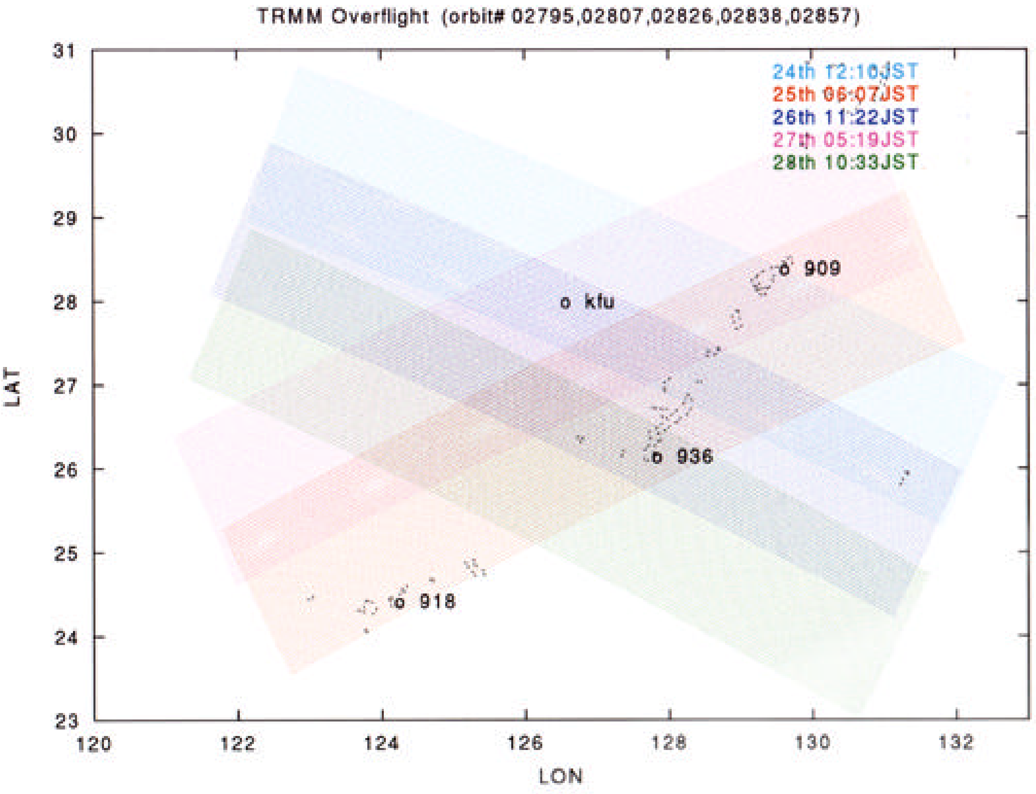

Fig. 5.8 TRMM PR observation for 24 to 28 May.

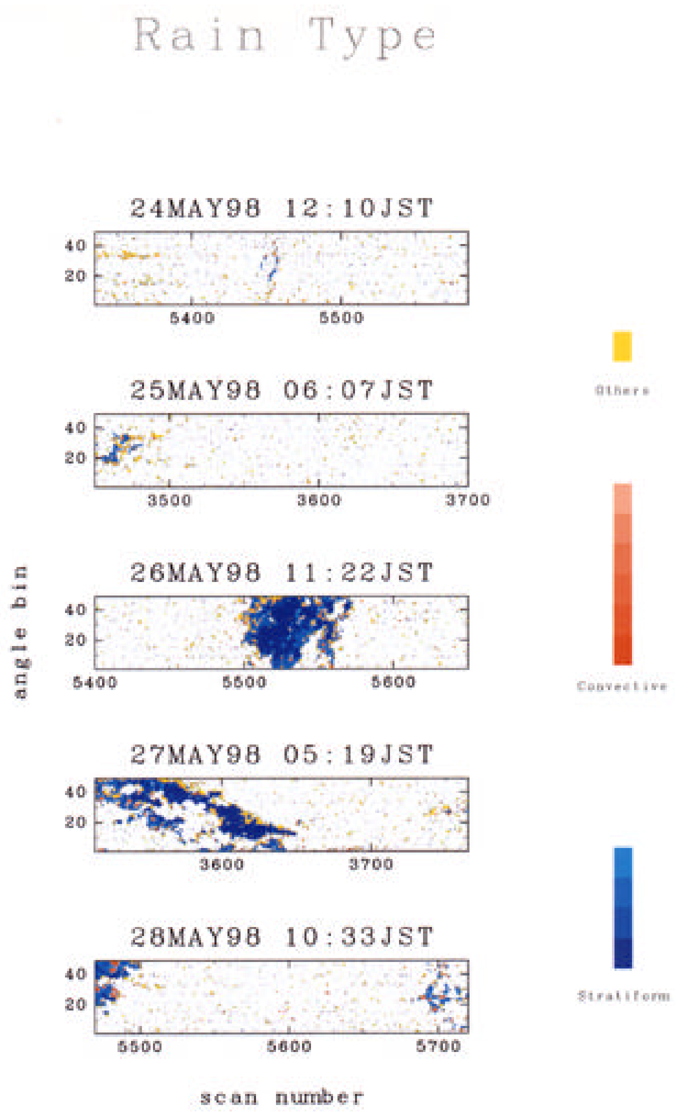

Fig. 5.9 Precipitation type observed by the PR.

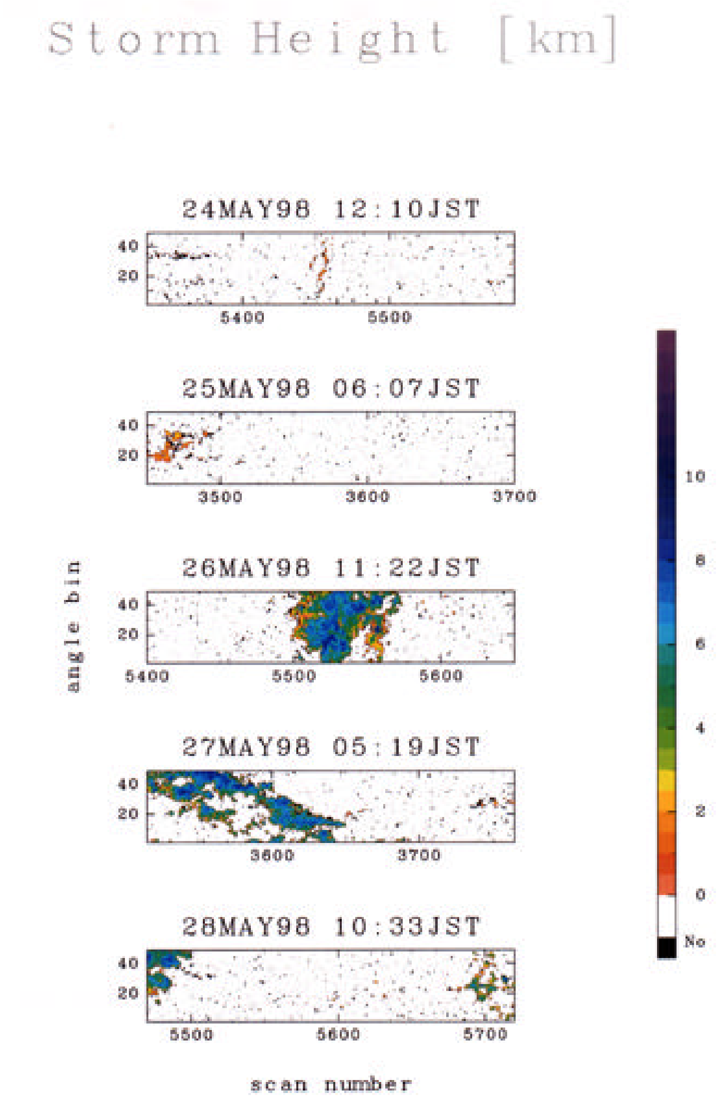

Fig. 5.10 Storm heights observed by the PR from 24 to 28 May.

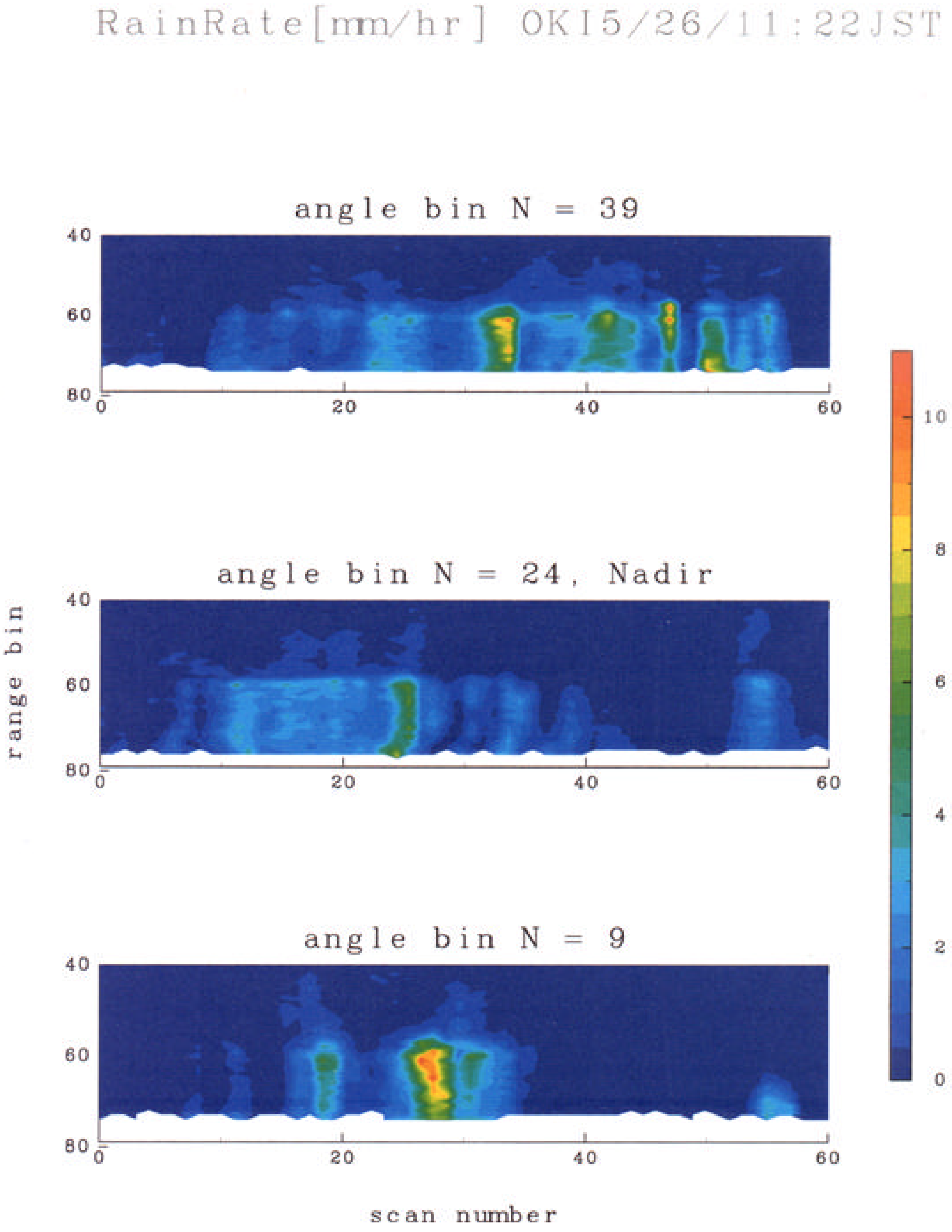

Fig. 5.11 Storm heights observed by the PR on 26 May.

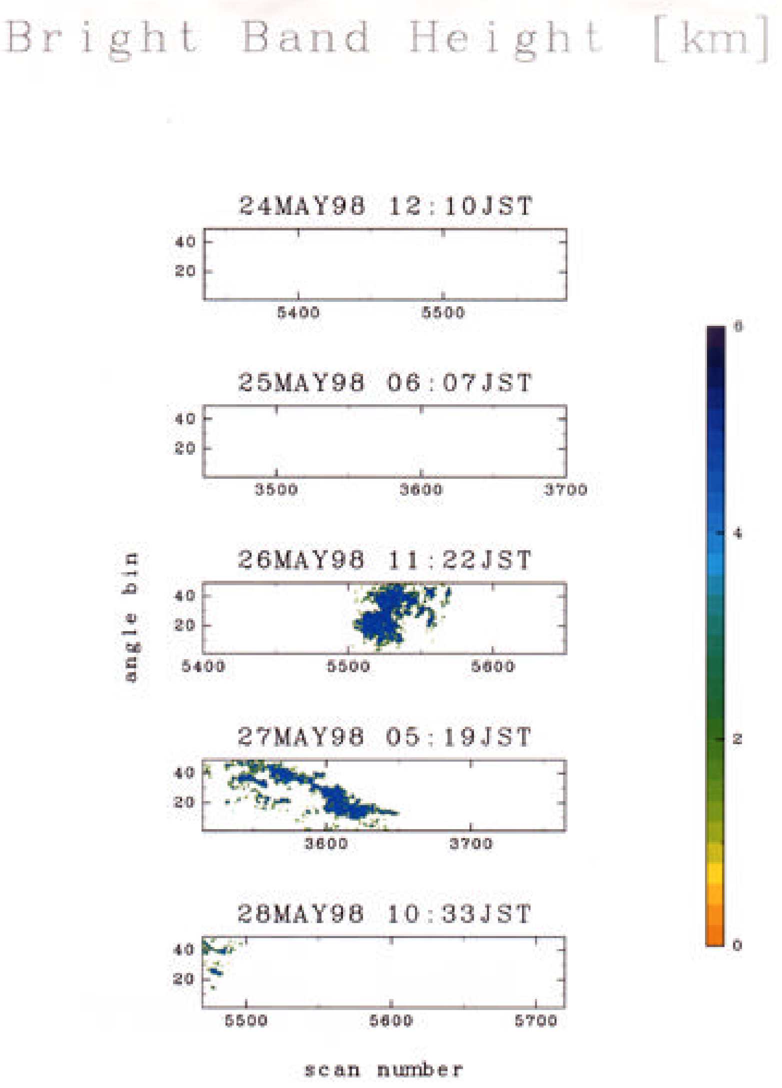

Fig. 5.12 Bright band height observed by the PR from 24 to 28 May.

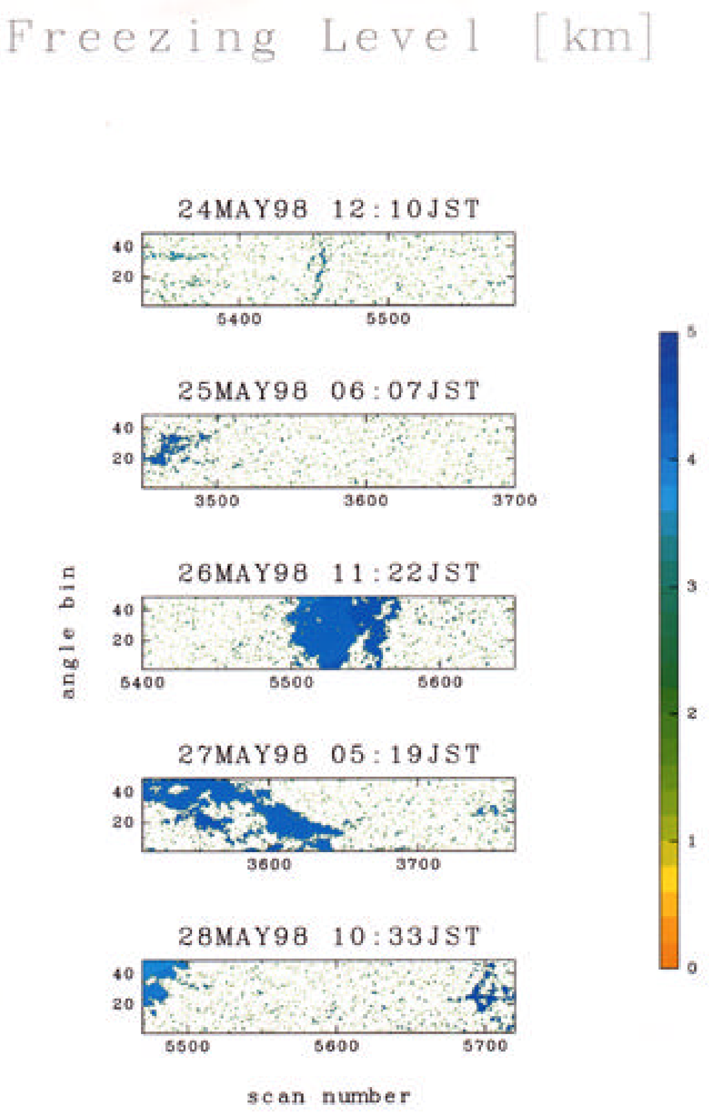

Fig. 5.13 Freezing levels observed by the PR from 24 to 28 May.

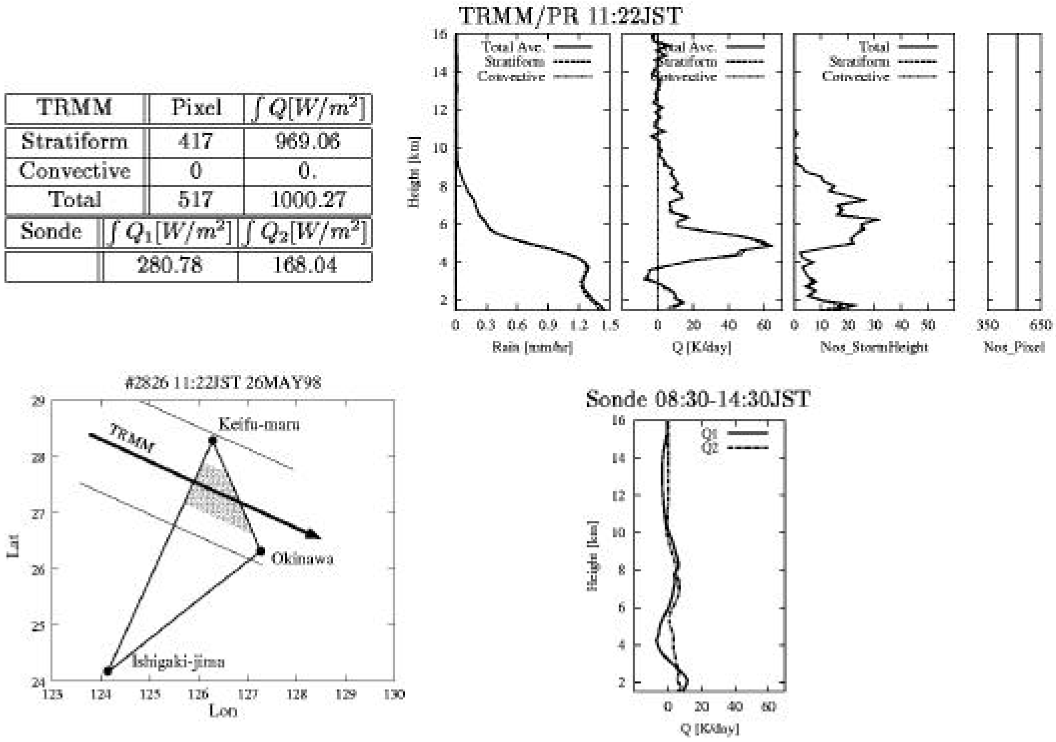

TRMM	Pixel	$\int Q[W/m^2]$
Stratiform	417	969.06
Convective	0	0.
Total	517	1000.27
Sonde	$\int Q_1[W/m^2]$	$\int Q_2[W/m^2]$
	280.78	168.04

Fig. 5.14 (a) Vertical structure of rain rate, Q1 and Q2 averaged over the area (A, 26May).

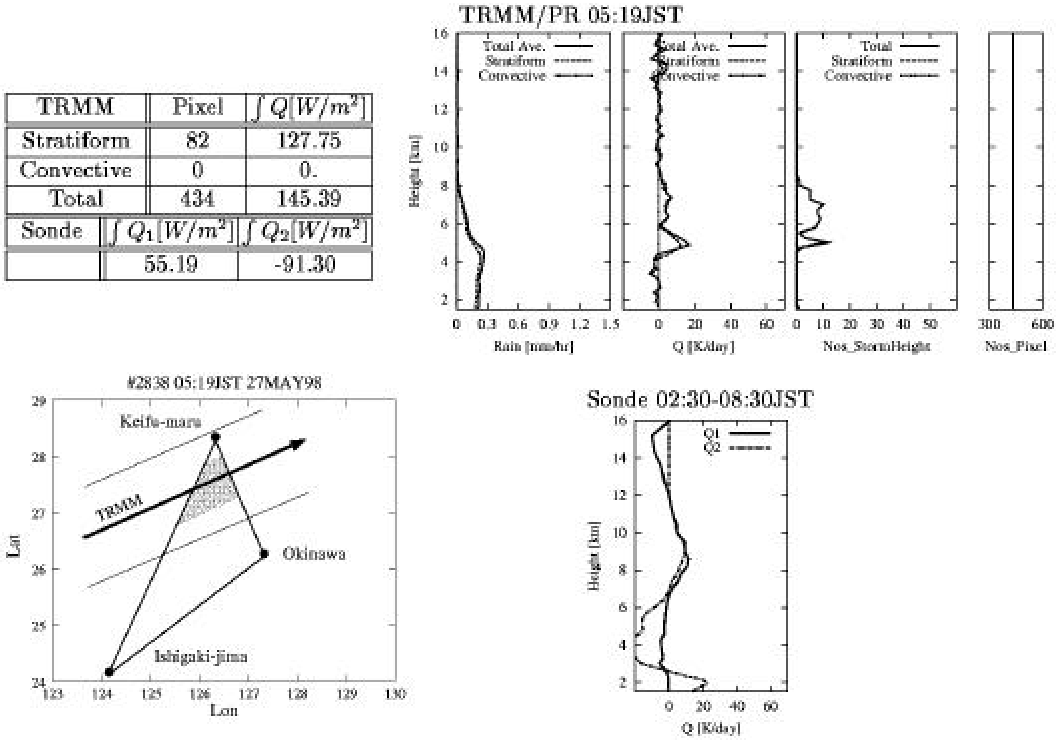

TRMM	Pixel	$\int Q[W/m^2]$
Stratiform	82	127.75
Convective	0	0.
Total	434	145.39
Sonde	$\int Q_1[W/m^2]$	$\int Q_2[W/m^2]$
	55.19	-91.30

Fig. 5.14 (b) Vertical structure of rain rate, Q1 and Q2 averaged over the area (A, 27May).

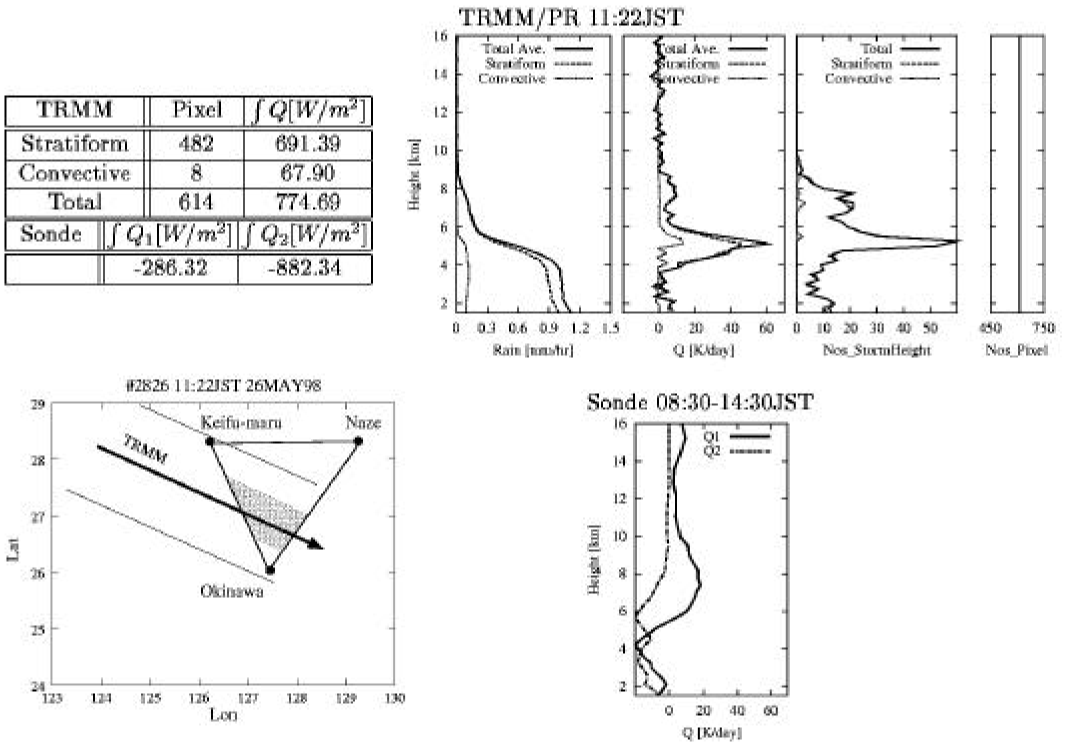

TRMM	Pixel	$\int Q[W/m^2]$
Stratiform	482	691.39
Convective	8	67.90
Total	614	774.69
Sonde	$\int Q_1[W/m^2]$	$\int Q_2[W/m^2]$
	-286.32	-882.34

Fig. 5.14 (c) Vertical structure of rain rate, Q1 and Q2 averaged over the area (B, 26May).

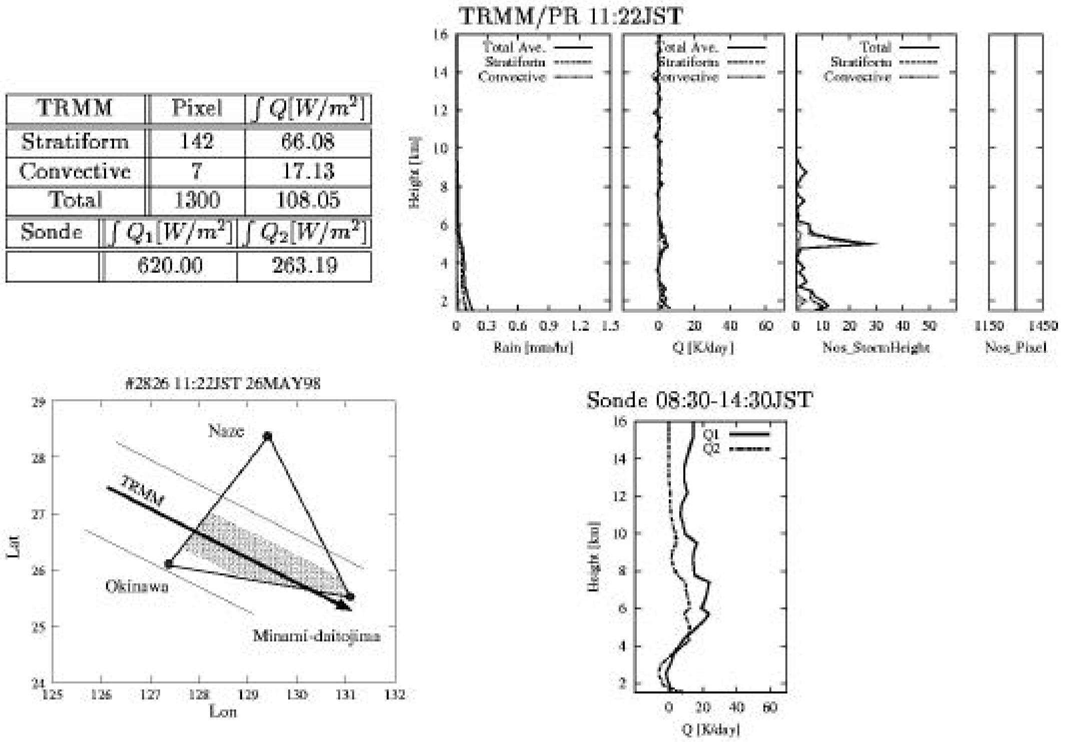

TRMM	Pixel	$\int Q[W/m^2]$
Stratiform	142	66.08
Convective	7	17.13
Total	1300	108.05
Sonde	$\int Q_1[W/m^2]$	$\int Q_2[W/m^2]$
	620.00	263.19

Fig. 5.14 (d) Vertical structure of rain rate, Q1 and Q2 averaged over the area (C, 26May).

6. Other data observed in IMCET' 98

Kinji Furukawa : National Space Development Agency of Japan

6.1 Comparison of the PR with Ishigakijima and Okinawa radar.

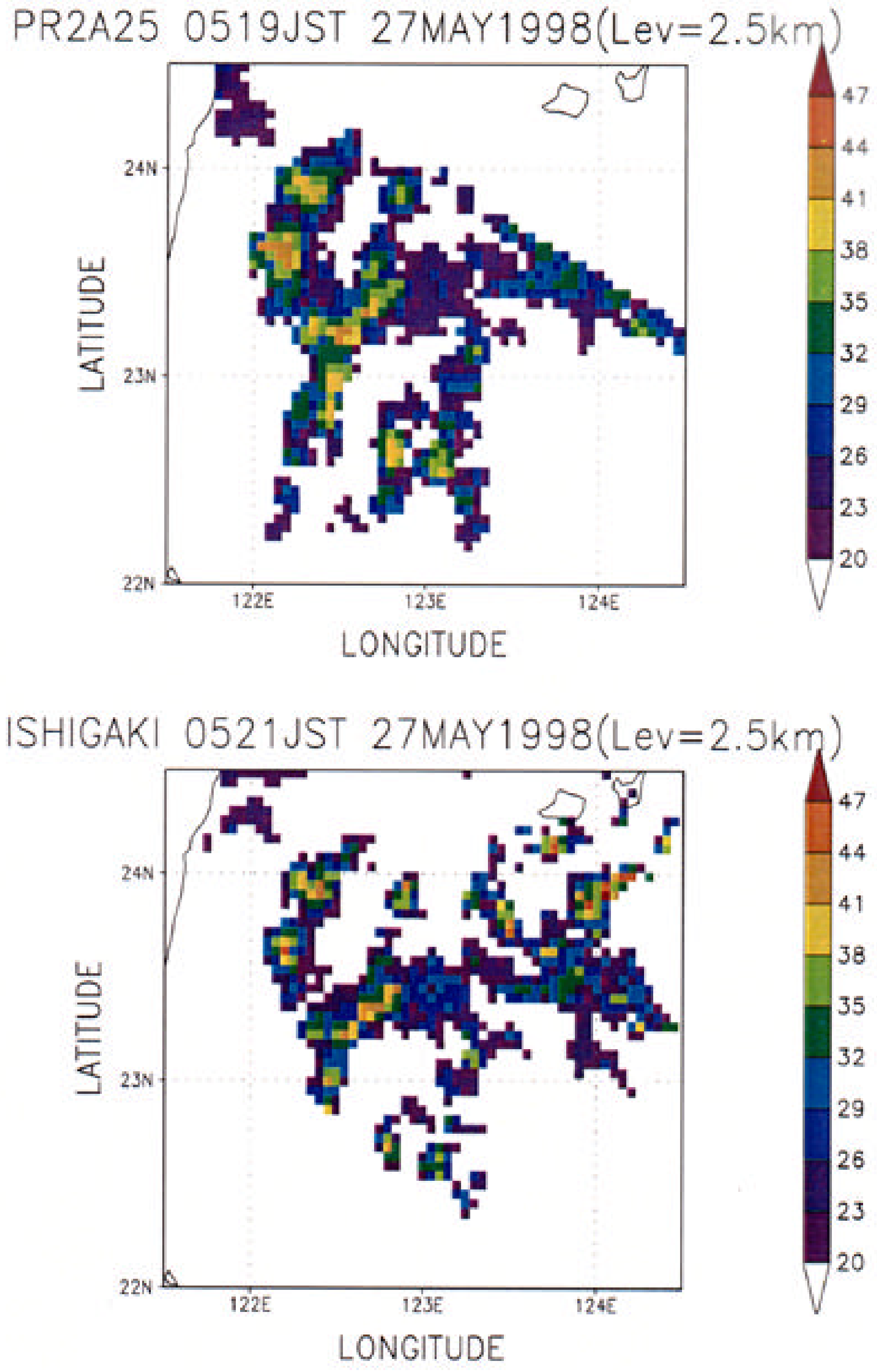

Fig. 6.1 Horizontal pattern of radar reflectivity (attenuation corrected) by the PR (a) and Ishigakijima ground based radar (b) at 2.5km height on May 27, 1998 at around 05:20

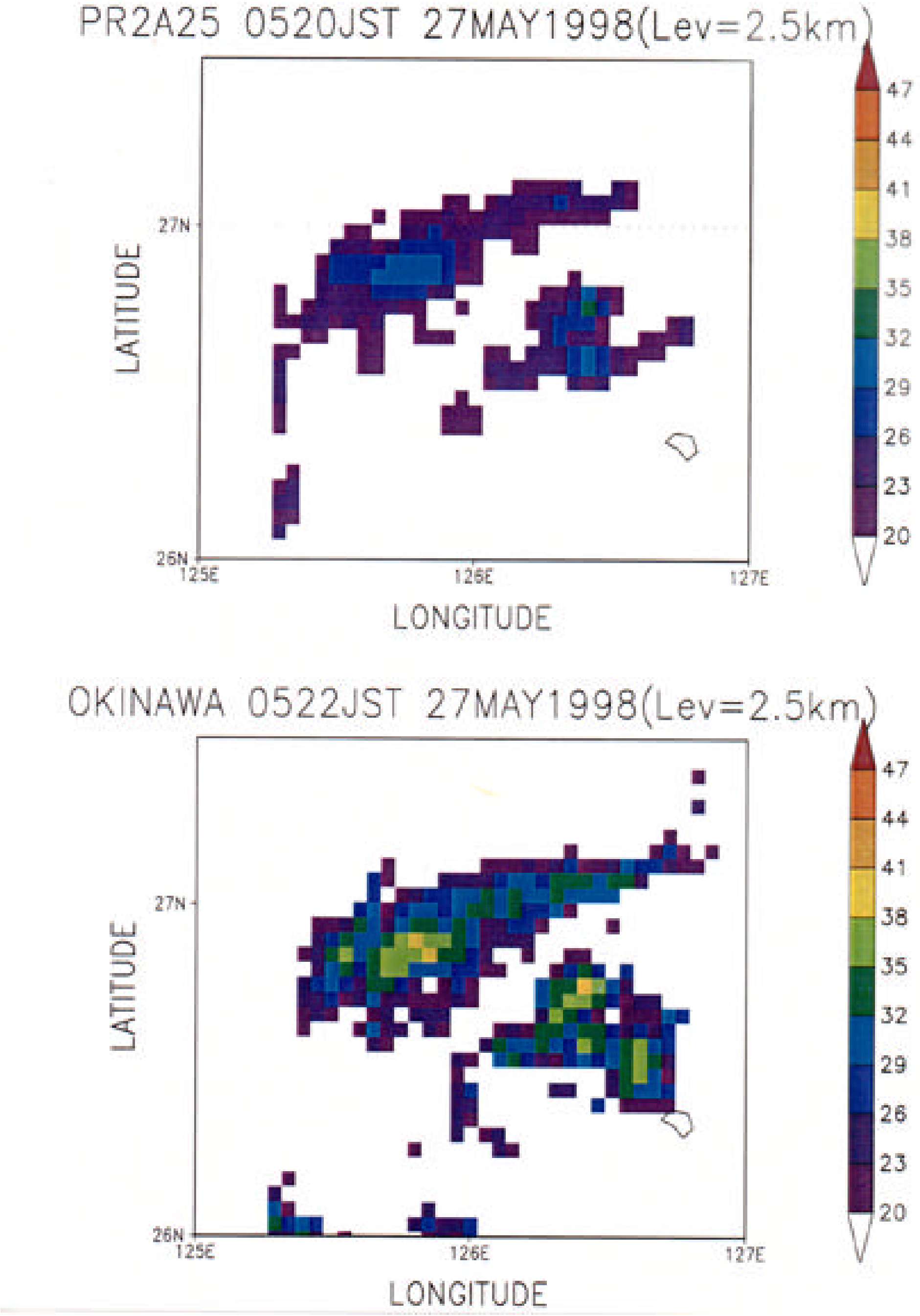

Fig. 6.2 Horizontal pattern of radar reflectivity (attenuation corrected) by the PR (a) and Okinawa ground based radar (b) at 2.5km height on May 27, 1998 around 05:22

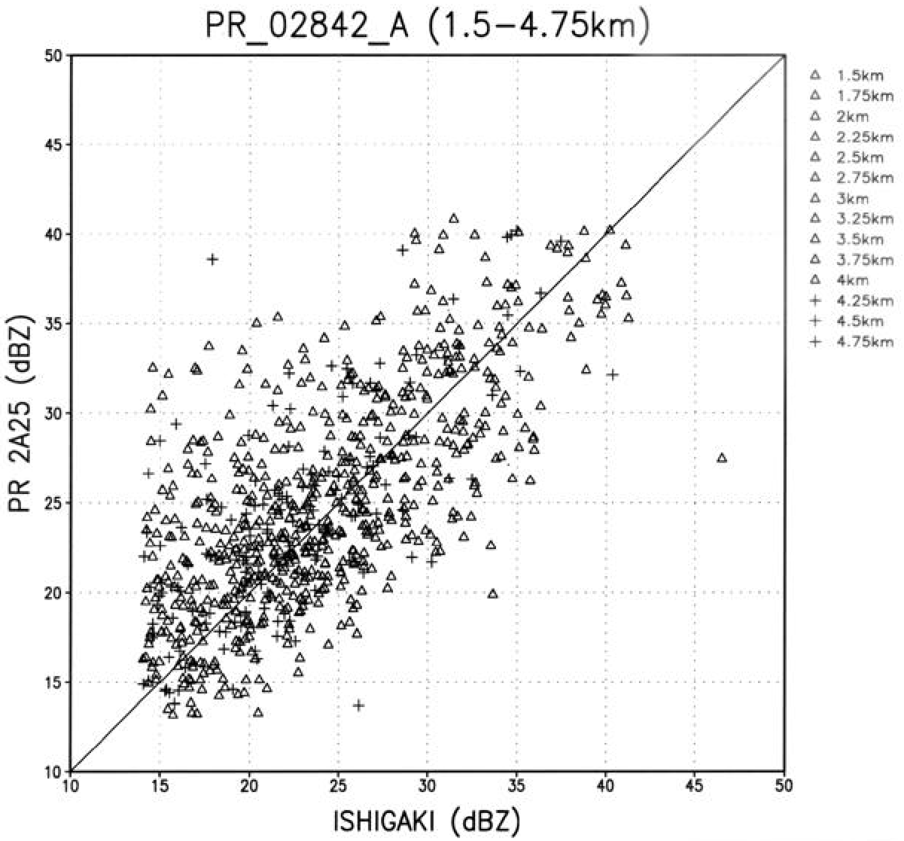

Fig. 6.3 Scatter diagram of the radar reflectivity for the PR and Ishigakijima radar for the case indicated in the Fig. 6.1

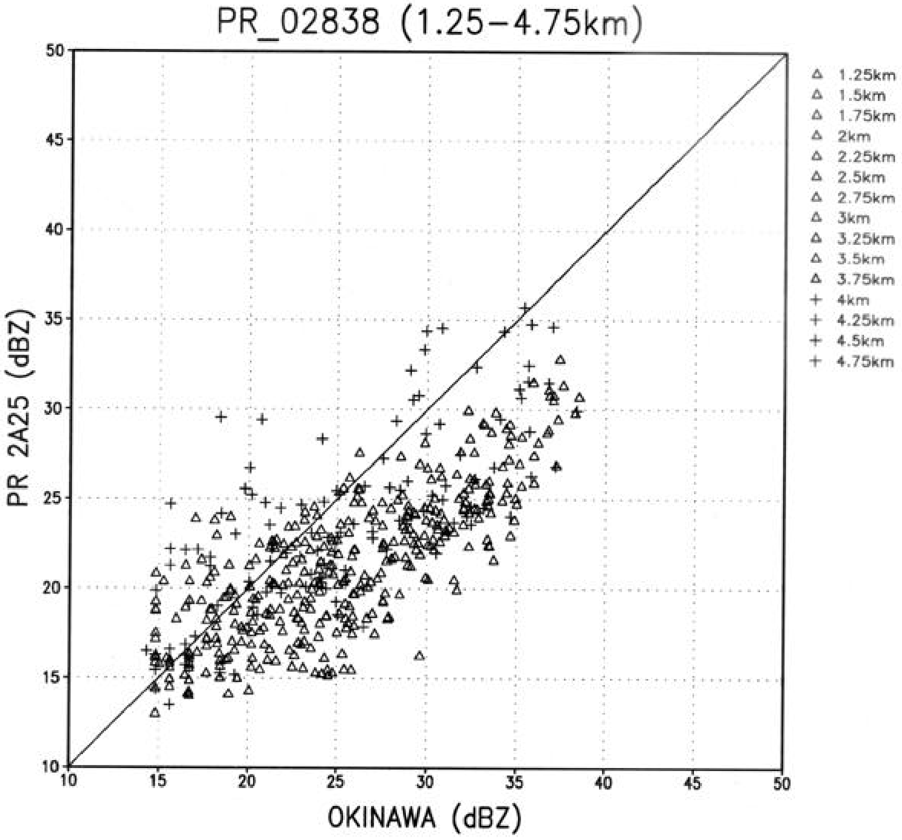

Fig. 6.4 Scatter diagram of the radar reflectivity for the PR and Okinawa radar for the case indicated in the Fig. 6.2

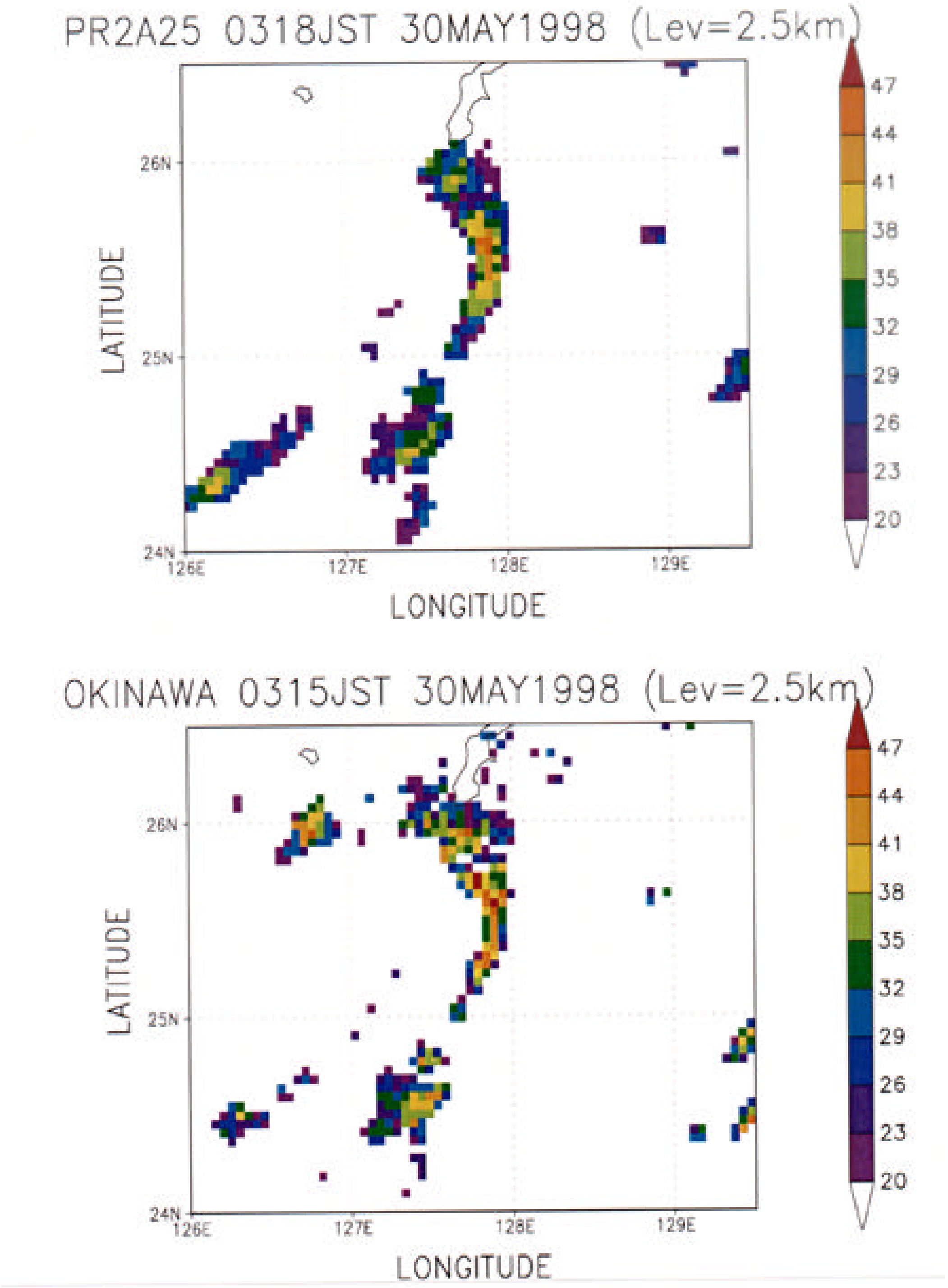

Fig. 6.5 Same as Fig. 6.2 on May 30, 1998 at around 03:17

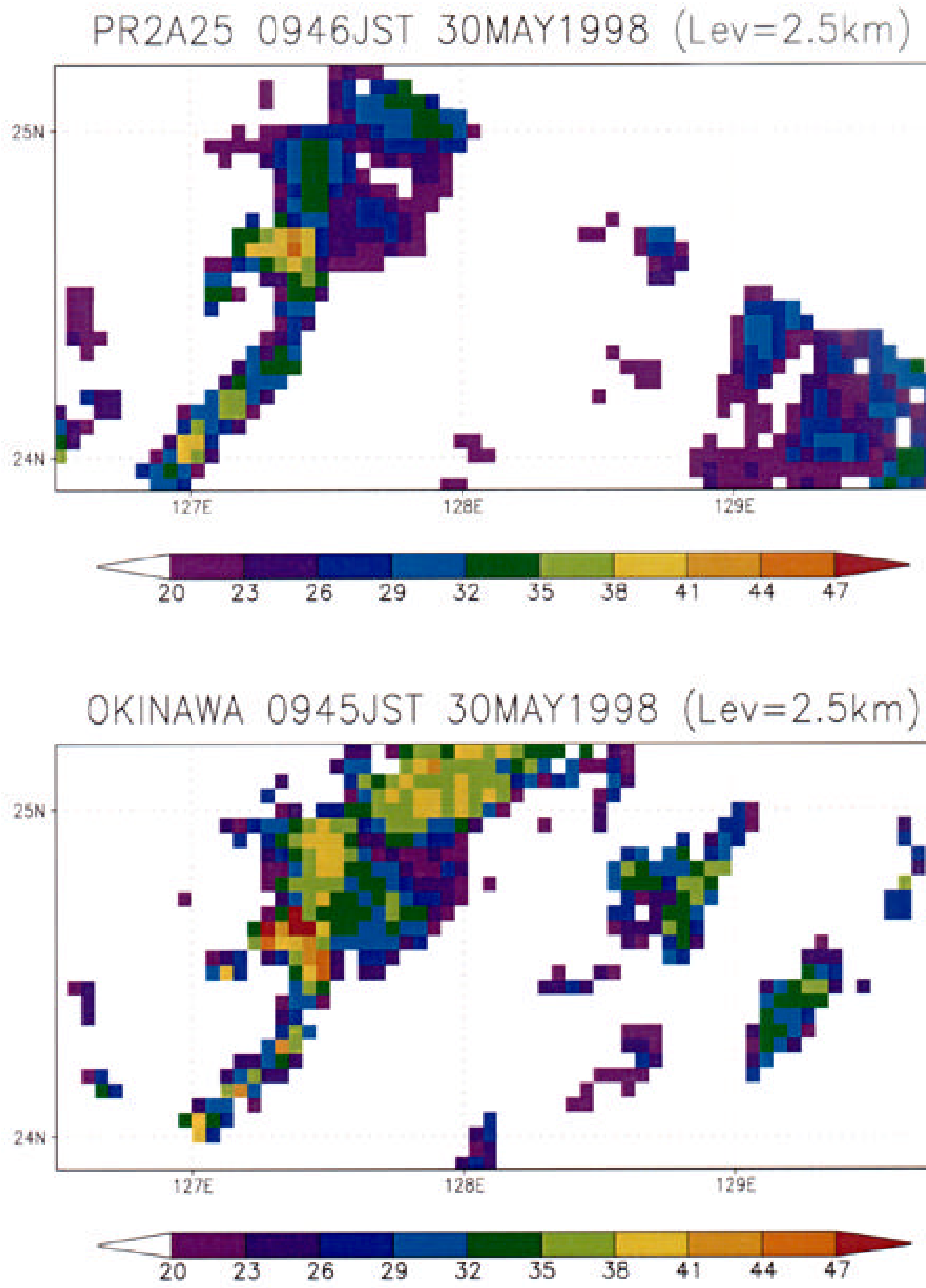

Fig. 6.6 Same as Fig. 6.2 on May 30, 1998 around 09:45

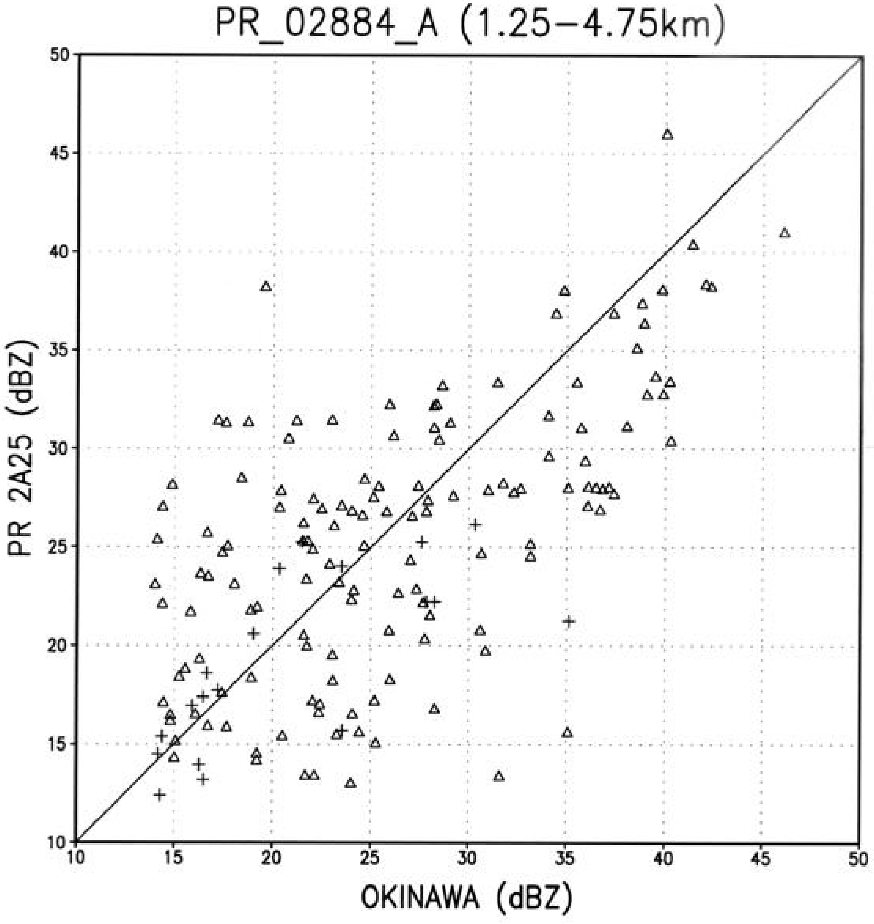

Fig. 6.7 Same as Fig. 6.4 for the case indicated in the Fig. 6.5.

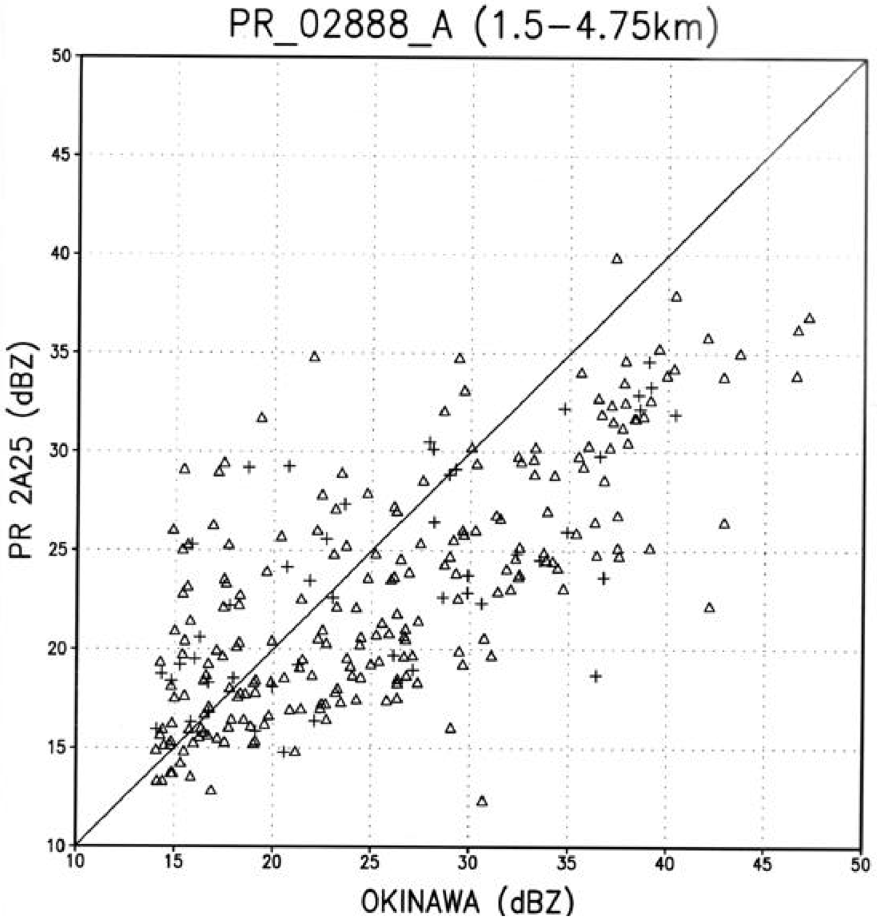

Fig. 6.8 Same as Fig. 6.4 for the case indicated in the Fig. 6.6.

6.2 Comparison of the PR with Keifumaru radar.

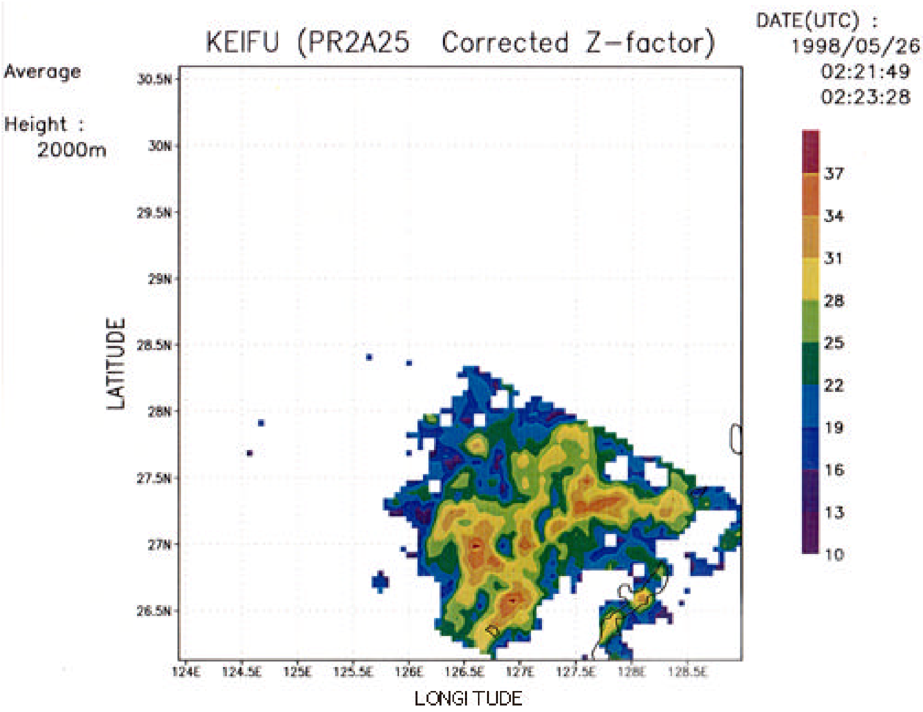

Fig. 6.9 Horizontal pattern of radar reflectivity (attenuation corrected) by the PR at 2.0km height on May 26, 1998 around 05:23.

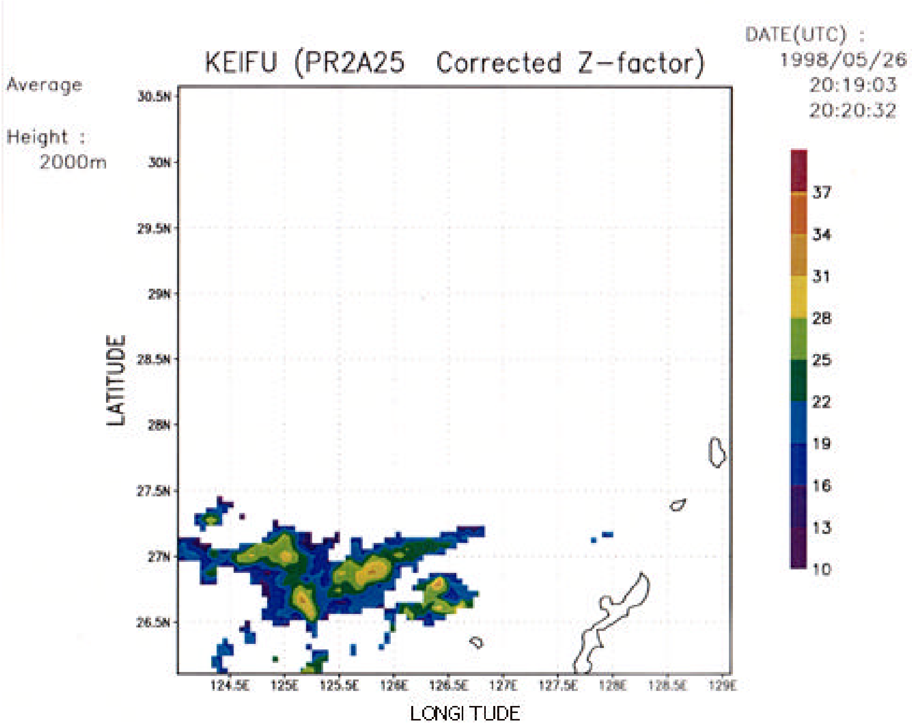

Fig. 6.10 Same as Fig. 6.9 on May 26, 1998 around 20:20.

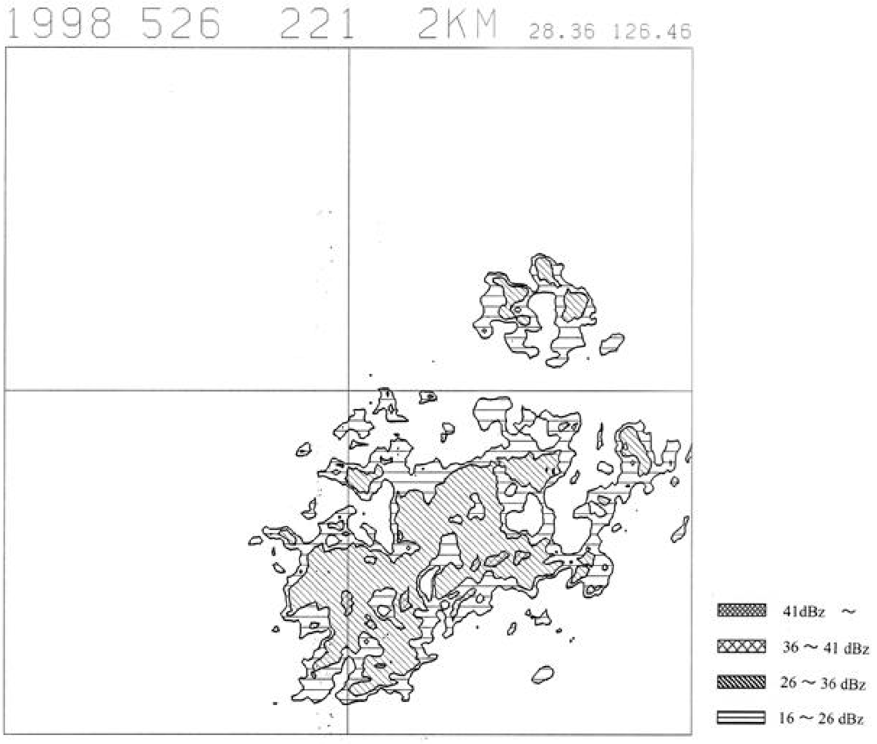

Fig. 6.11 Horizontal pattern of radar reflectivity by Keifumaru at 2.0 km height on May 26, 1998 around 05:23

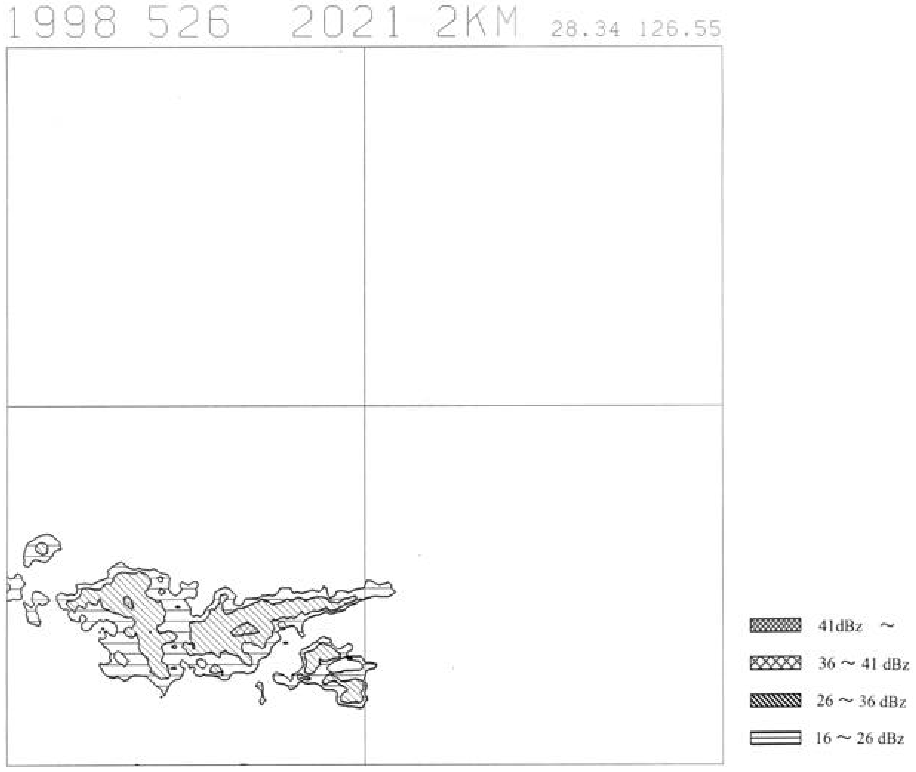

Fig. 6.12 Same as Fig.6.11 on May 26, 1998 around 20:20

6.3 Microwave radiometer observation.

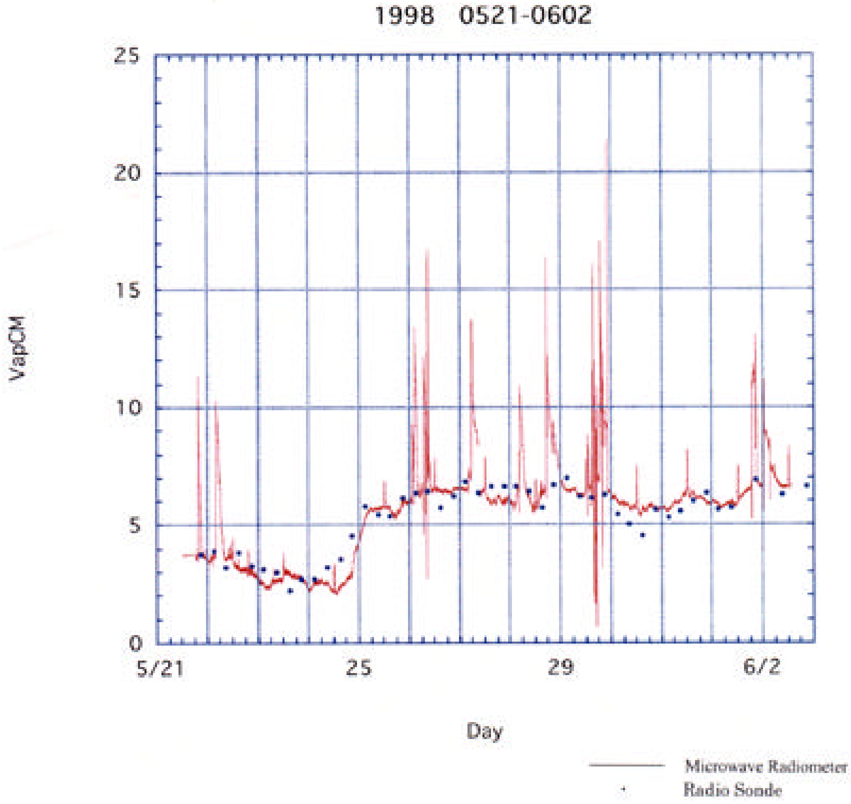

Fig. 6.13 Water vapor content retrieved from the microwave radiometer data and from upper air sounding at Ishigakijima.

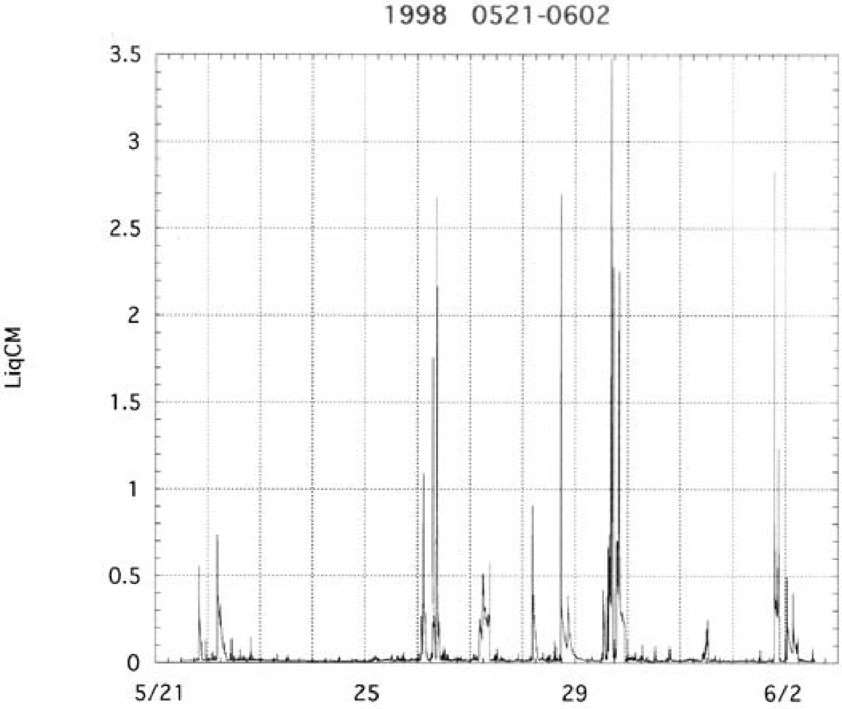

Fig. 6.14 Cloud liquid water retrieved from the microwave radiometer data

6.4 Surface observation

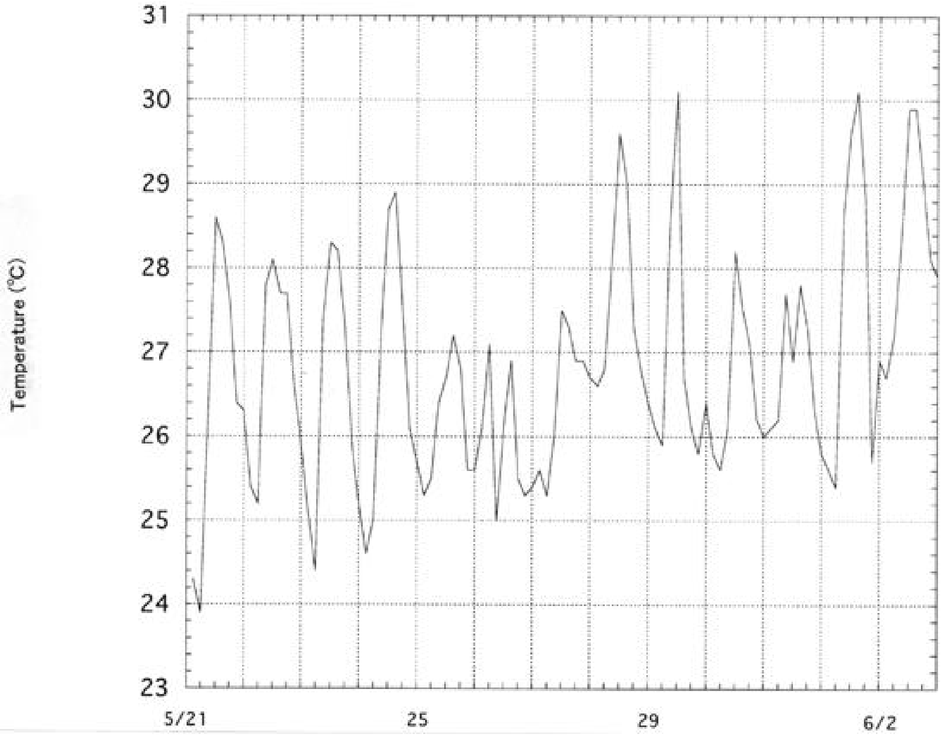

Fig. 6.15 Surface temperature at Miyakojima meteorological observatory.

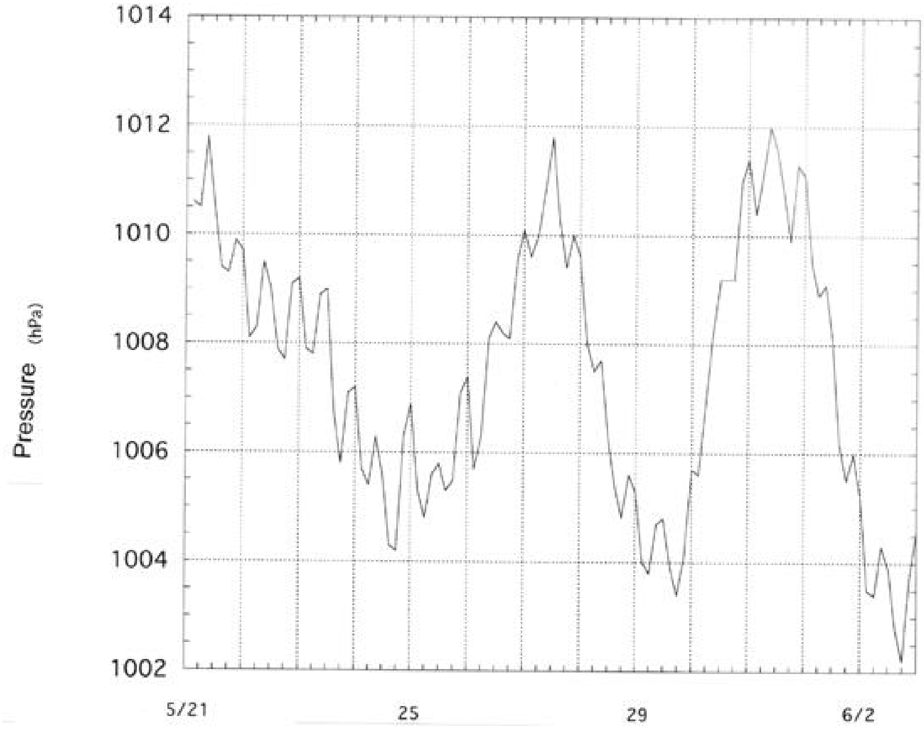

Fig. 6.16 Surface pressure at Miyakojima meteorological observatory.

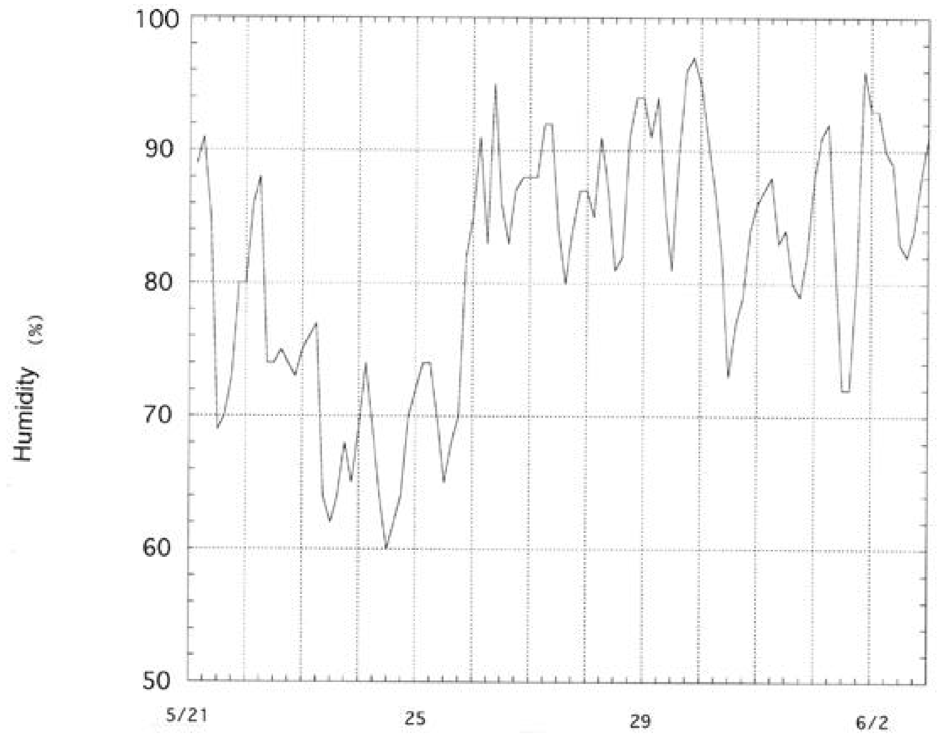

Fig. 6.17 Surface humidity at Miyakojima meteorological observatory.

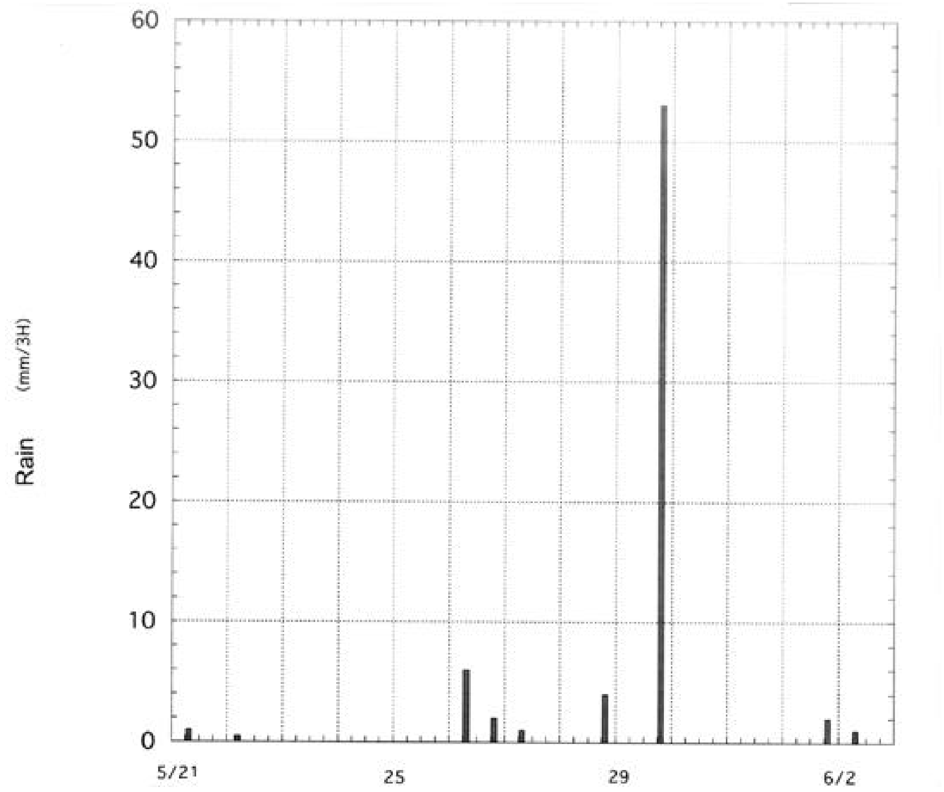

Fig. 6.18 Surface precipitation at Miyakojima meteorological observatory.